A distortional hardening model for finite plasticity

Citation for the original published paper (version of record):
Meyer, K., Menzel, A. (2021). A distortional hardening model for finite plasticity. International Journal of Solids and Structures, 232. http://dx.doi.org/10.1016/j.ijsolstr.2021.111055

International Journal of Solids and Structures 232 (2021) 111055

Contents lists available at ScienceDirect

International Journal of Solids and Structures

journal homepage: www.elsevier.com/locate/ijsolstr

A distortional hardening model for finite plasticity

Knut Andreas Meyer [a,*], Andreas Menzel [b,c]

[a] Division of Material and Computational Mechanics, Chalmers University of Technology, SE-41296 Gothenburg, Sweden
[b] Department of Mechanical Engineering, Institute of Mechanics, TU Dortmund, Dortmund D-44228, Germany
[c] Division of Solid Mechanics, Lund University, P.O. Box 118, Lund SE-22100, Sweden

ARTICLE INFO

Article history:
Received 7 September 2020
Received in revised form 12 April 2021
Accepted 14 April 2021
Available online 20 April 2021

Keywords:
Evolving anisotropy
Finite strain plasticity
Constitutive model
Pearlitic steel
Yield surface
Experimental mechanics

ABSTRACT

Plastic anisotropy may strongly affect the stress and strain response in metals subjected to multiaxial cyclic loading. This anisotropy evolves due to various microstructural features. We first use simple models to study how such features result in evolving plastic anisotropy. A subsequent analysis of existing distortional hardening models highlights the difference between stress- and strain-driven models. Following this analysis, we conclude that the stress-driven approach is most suitable and propose an improved stress-driven model. It is thermodynamically consistent and guarantees yield surface convexity. Many distortional hardening models in the literature do not fulfill the latter. In contrast, the model proposed in this work has a convex yield surface independent of its parameter values. Experimental results, considering yield surface evolution after large shear strains, are used to assess the model's performance. We carefully analyze the experiments in the finite strain setting, showing how the numerical results can be compared with the experimental results. The new model fits the experimental results significantly better than its predecessor without introducing additional material parameters.

1. Introduction

Capturing the evolving plastic anisotropy is essential in several industrial applications, such as sheet metal forming and rolling contact fatigue in railways. The foundation for modeling evolving anisotropy is found in earlier models that only consider a fixed anisotropy case, such as Papadopoulos and Lu (2001). However, Kweon (2013) showed that the evolution of plastic anisotropy strongly influences damage during shear loading. Within the last decades, several different models that describe the evolution of plastic anisotropy have been presented in the literature. These models range from micro-mechanical, via micro-mechanically motivated, to purely phenomenological models. Micro-mechanical models are useful in understanding the mechanisms occurring in the material's microstructure. Despite many recent efforts to decrease the computational costs, see e.g. Wicht et al. (2020), they are still too computationally demanding for many industrial applications. The models discussed in the present work are, therefore, mainly micro-mechanically motivated or purely phenomenological.

Since the early works by Naghdi et al. (1958), the effect of plastic deformation on subsequent yield surfaces has been investigated in many studies. Many studies, such as, e.g., Ishikawa and Sasaki (1988), Sung et al. (2011), Yang et al. (2018) attempt to capture the true yield surfaces. In this context, the true yield surface refers to stresses at which plasticity starts to evolve. When studying sheet metals, see, e.g., Banabic et al. (2003), Barlat et al. (2005), Dunand et al. (2012), a large plastic offset is typically employed. These studies capture yield surfaces that describe the stresses at a certain amount of plastic deformation. Both types of studies show that the shape of the yield surface evolves during plastic deformation.

The paper is organized as follows: Section 2 provides a microstructural motivation for distortional hardening. The purpose of this section is to highlight mechanisms that distortional hardening models should include. In Section 3, a review of different modeling approaches is given. In particular, this section serves as a motivation for choosing the so-called "stress-driven" modeling approach. The improved model, motivated by the previous sections, is then presented in Section 4. The model's ability to fit and predict the experimental data from Meyer et al. (2020) is investigated in Section 5.

2. Microstructural motivation for anisotropic yield surfaces

In general, the observed macroscopic material behavior is a result of different deformation processes at the micro-scale. The

* Corresponding author.
E-mail address: knut.andreas.meyer@chalmers.se (K.A. Meyer).

https://doi.org/10.1016/j.ijsolstr.2021.111055
0020-7683/

specific material investigated in the present study is a pearlitic railway steel. It consists of hard cementite lamella embedded in a softer ferrite matrix (see Fig. 1). It is thus a composite material consisting of hard and soft phases with different crystallographic textures. The purpose of this section is to provide a physical motivation for the development of the constitutive model. To that end, we analyze the deformation processes on the microscale. The main emphasis of the discussion is on pearlitic steel. However, most other metal alloys also have a multi-phase composition in addition to the crystal structure. Hence, the following discussion is also relevant for metals in general.

2.1. The Masing effect

Bauschinger (1881) first reported the decrease in yield limit upon loading in the reversed direction (Abel and Muir, 1972). Forty-five years later, Masing (1926) presented a model that could explain this effect (Skelton et al., 1997). Masing's model consists of perfectly plastic bars with different yield limits. When subjecting these bars to the same strain, the yield stress upon load reversal decreases. We will now simulate a dual-phase material to investigate this effect. The elastic behavior of each phase is linear, while the plastic behavior is non-linear isotropically hardening. All material parameters are equal, except for the initial yield limit. It is 300 ± 100 MPa for the dual-phase material and 300 MPa for the single-phase material. Fig. 3a shows the yield surface after a tensile uniaxial predeformation. For the dual-phase material, the yield surface is translated (as was also observed by Masing), but not distorted. Hence, we conclude that the Masing effect results in a distortion-free translation of the yield surface.

2.2. Polarization of dislocations

Another explanation for the Bauschinger effect is the polarization of the dislocations, see e.g. Kocks and Mecking (2003). This polarization causes reduced resistance to yielding upon reversal of the resolved shear stress. Such a process can be simulated by using a crystal plasticity framework in which each slip system has its back-stress. Amongst others, Méric et al. (1991) proposed such a model. In this study, we adopt the Taylor homogenized model from Meyer (2020). That model consists of 32 uniformly oriented grains, which are all subjected to the same strain. The uniform orientation was obtained following Quey et al. (2018). Fig. 3b shows that the initial yield surface is nearly isotropic for this model.

The dislocation polarization is driven by a uniaxial tensile predeformation. We first consider the model with zero hardening ($H = 0$), such that each slip system is perfect elasto-plastic. In this case, the model consists of a collection of crystals with different orientations. The crystals have different yield limits in the particular loading direction, and a Masing-type effect is expected. However, the result in Fig. 3b shows that the yield surface distorts in addition to slightly translating. When introducing the kinematic hardening ($H_{\text{kin}} \neq 0$) on the slip systems, both the translation and distortion amplifies. When introducing isotropic hardening ($H_{\text{iso}} \neq 0$) instead, similar translation and distortion to the ideal plastic case occur.

It is important to note here that many different approaches to crystal plasticity modeling are available in the literature. One example is Barrett et al. (2020). They use the self-consistent homogenization approach and a different kinematic hardening formulation. A 3D RVE, such as in Zhang et al. (2016), is the most accurate approach. However, similar results to those in Fig. 3b were observed in e.g. Jeong et al. (2017).

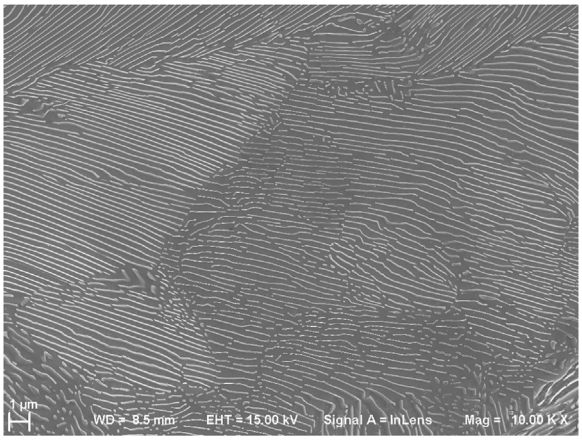

Fig. 1. Scanning Electron Microscope image showing the pearlitic microstructure, which consists of cementite lamellas (light contrast) embedded in a ferrite matrix (dark contrast).

2.3. Elastic inclusions

The cementite lamellas have a higher yield limit compared to the ferrite matrix. It is, therefore, instructive to consider an elliptic elastic inclusion within an elasto-plastic isotropically hardening matrix. Fig. 2 shows the result of such a simulation, conducted under the assumption of plane stress. Periodic boundary conditions are used. By loading the Representative Volume Element (RVE) in different combinations of normal and shear loading, a yield surface can be measured in the $\sigma_{zz} - \sigma_{z\theta}$ plane. Fig. 3c shows the resulting yield surface. When no sliding between the inclusion and the surrounding matrix is allowed, there is no effect from the inclusion. As the elastic properties are equal, the onset of yielding is not affected by the inclusion. Large differences in the elastic stiffness only cause a slight anisotropic yield surface. Considering that the stiffness of the cementite is of the same order of magnitude as the ferrite (Ghosh, 2015), this effect is likely negligible. However, allowing the inclusion to slide relative to the matrix results in a strongly anisotropic yield surface. We thus conclude that the interface behavior between inclusions and matrix strongly influences the anisotropic yield behavior. An important observation is that the yield surface is double symmetric around the origin. This symmetry is not existing in the distortion after the Masing effect or the polarization of dislocations discussed above.

In this example, a single inclusion was considered. Macroscopic anisotropy requires that there is a preferred alignment of the inclusions. Such alignment may occur as inclusions reorient due to plastic flow in the matrix material. How this reorientation evolves is also strongly connected to the interface between the inclusion and the matrix.

2.4. Single crystal yielding

A common explanation for deformation-induced anisotropy is the reorientation of the crystallographic texture. Each grain has a pronounced plastic anisotropy, as is shown for a BCC crystal in Fig. 3d. As was observed for the elastic inclusion above, the response is double-symmetric around the origin. As shown analytically by Dafalias (1993), the grains align with deformation and the macroscopic response approaches to that of the single crystal. The crystals also have anisotropic elastic properties. As the grains align, both the elastic and the plastic material response become anisotropic, following the ideas by, e.g., Man (1995) and Böhlke and Bertram (2001).

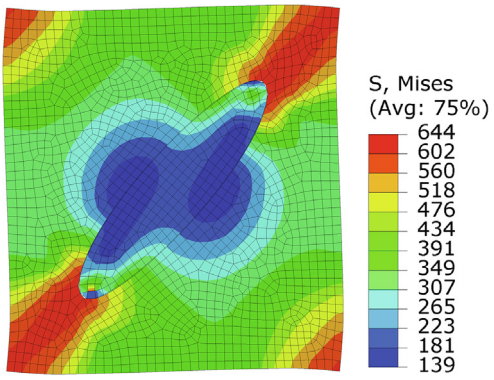

Fig. 2. Compression of an RVE with an elastic inclusion (periodic boundary conditions).

2.5. Summary of microstructural motivation

In this section, four deformation mechanisms on the microstructure, affecting the anisotropic yielding behavior, have been identified. From these analyses, we conclude that three effects should be considered:

1. The translation of the yield surface due to the Masing effect.
2. The asymmetric distortion of the yield surface due to the polarization of dislocations and the Masing effect on crystal yielding (this is also denoted directional distortion).
3. The symmetric distortion of the yield surface due to the evolution of inclusion and grain orientation.

3. Review of established models

Many different models for distortional hardening have been proposed in the literature. One way to differentiate between models is whether the anisotropy evolution is connected to the strains (plastic or total) or evolves separately as a function of the stress history. Below, we briefly review these different approaches with some examples from the literature. The goal of this comparison is to motivate the choices made for the improved model presented in Section 4.

3.1. Strain-driven models

Typically, the "strain-driven" models obtain anisotropic responses based on the evolution of the microstructure, which is described by microstructural features such as orientation distribu-

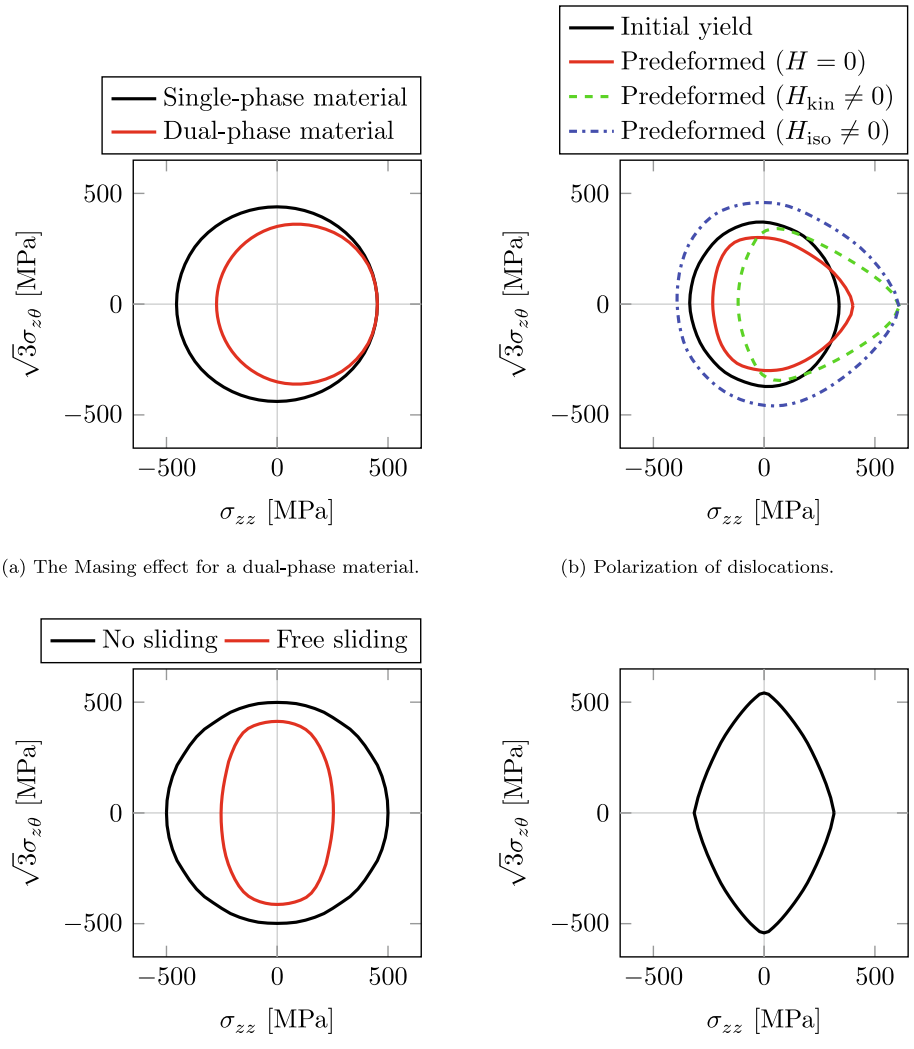

(a) The Masing effect for a dual-phase material.

(b) Polarization of dislocations.

(c) Effect of an elastic inclusion.

(d) Single crystal yielding.

Fig. 3. Yield surfaces due to different physical mechanisms. All stress components, except $\sigma_{\theta z} = \sigma_{z\theta}$ and σ_{zz}, are zero.

tions of crystals or inclusions. The evolution of the orientation distributions can either be due to affine (following the deformation) or non-affine (adding additional degrees of freedom) reorientation of the microstructural features. The latter is conceptually related to the plastic spin, see e.g. Dafalias (2001). Dafalias (1985), based on the requirement on objectivity stated in Mandel (1971) and Kratochvil (1971), proposed constitutive relations for this spin. Mandel (1971) and Kratochvil (1971) introduced the need for constitutive relations for the plastic spin. Later, Dafalias (1985) proposed a general formulation for such constitutive relations "based on the invariance requirements and the representation theorems for isotropic functions (Dafalias, 1983)". Those constitutive relations govern the spin of the intermediate configuration, which is of particular interest for anisotropic models. Dafalias and Rashid (1989) give an in-depth discussion on the influence of the plastic spin on anisotropic models. However, Wallin and Ristinmaa (2005) also showed that the plastic spin affects the Swift effect, Swift (1947), for a model with a yield surface that is isotropic with respect to the reduced stress (difference between the stress and the back-stresses due to kinematic hardening). Note that the kinematic hardening makes that model anisotropic. This feature explains why the plastic spin affects the Swift effect at large deformations, as shown analytically by Dafalias (1985).

An advantage with the strain driven approach is the models' connection to the microstructure. Along these lines, Man (1995) proposed that the anisotropy coefficients for the yield criterion are related to the elastic anisotropy coefficients. Böhlke and Bertram (2001) further developed this idea by proposing a model in which the elastic and plastic anisotropy evolve following the plastic strains.

Many models in the literature introduce anisotropy via microstructure evolution, see e.g. Menzel and Steinmann (2003), Lu and Papadopoulos (2004), Johansson et al. (2005), Johansson and Ekh (2006), HHarrysson and Ristinmaa (2008), Kaiser et al. (2020). The microstructure is often described by a set of direction vectors, representing orientation distributions. In order to obtain a macroscopic model, these directions must be homogenized to build up structural tensors, which are used in, e.g., the yield criterion. To illustrate this process, we have chosen the model by Larijani et al. (2013), as it can be evaluated without fitting the full material response. We further enhance the evolution by allowing for non-affine transformation, following Dafalias (2001).

The yield criterion in Larijani et al. (2013) is designed for pearlitic steel, based on the resolved shear stress on cementite lamellas, see Fig. 1. Each lamella is described by a unit vector, $\underline{\boldsymbol{n}}$, and based on Larijani et al. (2013) we use the effective stress σ^{eff}

$$\sigma^{\text{eff}} = \sqrt{\boldsymbol{a} : [\boldsymbol{\sigma}\boldsymbol{\sigma}] - \boldsymbol{\sigma} : \mathbf{B} : \boldsymbol{\sigma}} \tag{1}$$

$$\boldsymbol{a} = \langle \underline{\boldsymbol{n}} \otimes \underline{\boldsymbol{n}} \rangle \tag{2}$$

$$\mathbf{B} = \langle \underline{\boldsymbol{n}} \otimes \underline{\boldsymbol{n}} \otimes \underline{\boldsymbol{n}} \otimes \underline{\boldsymbol{n}} \rangle \tag{3}$$

$$\langle \bullet \rangle = \frac{1}{4\pi} \int_{\text{sphere}} \bullet \, \mathrm{d}A \tag{4}$$

The integration over the sphere is done numerically using 10^4 random orientations. Following Dafalias (2001), the evolution of each cementite lamella is described by

$$\dot{\underline{\boldsymbol{n}}} = [\boldsymbol{W} - \eta[[\underline{\boldsymbol{n}} \otimes \underline{\boldsymbol{n}}]\boldsymbol{D} - \boldsymbol{D}[\underline{\boldsymbol{n}} \otimes \underline{\boldsymbol{n}}]]] \tag{5}$$

where $\boldsymbol{D} = 0.5[\boldsymbol{L} + \boldsymbol{L}^{\text{t}}]$, $\boldsymbol{W} = 0.5[\boldsymbol{L} - \boldsymbol{L}^{\text{t}}]$, and $\boldsymbol{L} = \dot{\boldsymbol{F}}\boldsymbol{F}^{-1}$. The parameter η controls the type of evolution, and $\eta = -1$ corresponds to the areal-affine reorientation used in Larijani et al. (2013).

For the smaller predeformation levels (Fig. 4b and c), the predicted degree of anisotropy is lower than in the experiments. At the maximum predeformation level (Fig. 4d), the degree of anisotropy is reasonable for $\eta = -1.0$ and $\eta = -1.5$. However, the rotation is incorrectly described. $0 > \eta > -1$ gives less distortion, while $\eta < -1$ gives more distortion than pure areal affine. In Meyer et al. (2020), Fig. 11a, the degree of anisotropy was shown to develop rather quickly and then saturate. For a high dissipation limit, the degree of anisotropy saturates already after one predeformation cycle (note that the results in Fig. 4 are for the low dissipation limit). The model results in Fig. 4b show almost no yield surface evolution, even for $\eta = -2.0$. From a physical point of view, it is questionable to use values of η that severely deviate from the areal-affine value of -1. In Meyer et al. (2015), the experimentally determined cementite re-orientation during wire drawing was reasonable for $-1 > \eta > -2$. In summary, it seems that the evolution of cementite lamellas is unable to fully describe the yield surface evolution in pearlitic steels. In particular, the strain driven approach predicts that the degree of anisotropy should keep increasing with increasing deformation. But in the experiments, this increase saturates rather quickly. The authors note, however, that many other microstructural features, such as crystal orientation, are also at play here. The above example is included to demonstrate some deficiencies with the strain-driven approach, which later motivate the use of the stress-driven approach.

Another disadvantage with the strain-driven approach is the difficulty in obtaining an efficient and accurate description of the microstructure orientation tensors. Larijani et al. (2013) used numerical integration based on Bažant and Oh (1986). On the other hand, Johansson and Ekh (2006) used closure approximations for the evolution of the structure tensors. In Appendix A, we compare these approaches, showing that each of them has several drawbacks. In particular, it appears to be difficult to combine high accuracy with an efficient numerical implementation. These findings further motivate us to consider stress-driven approaches.

3.2. Stress-driven models

As discussed above, the yield surface distortion in Meyer et al. (2020) developed rather quickly before saturating. Similar results were found in, e.g., Phillips and Juh-Ling (1972), where a relatively large yield surface distortion was found after only modest plastic strains. A region of high curvature develops in the pre-stressing direction, as is seen for crystal plasticity in Fig. 3b. To capture this effect was a focus of several early papers. A short-term evolution, remembering past stress states, was used, see Ortiz and Popov (1983). Several other authors have developed various models along similar lines, such as Voyiadjis and Foroozesh (1990), Wu et al. (1995), Kurtyka and Zyczkowski (1996). A common assumption in more recent models is that the current back-stress describes the direction of high curvature, see e.g. François (2001), Feigenbaum and Dafalias (2007), Noman et al. (2010), Pietryga et al. (2012), Shi et al. (2014). All models proposed in those papers worked reasonably well for the studied cases. However, as Plesek et al. (2010) bring up, there is no physical motivation for letting the direction of high curvature be aligned with the current back-stress.

Many works that use stress-driven evolution laws have dealt with the high curvature in the loading direction. However, most recent models also include cross- and self-hardening (sometimes referred to as latent and dynamic hardening, respectively), see e.g. Johansson et al. (2005), Noman et al. (2010), Pietryga et al. (2012), Shi et al. (2014). The cross- and self-hardening is often represented by a Hill-type yield surface. Such a quadratic yield surface was found to fit the experimental results in Meyer et al. (2020) well. In Meyer (2020), a slightly modified version of the model in Shi et al. (2014) was applied to those experimental results. Overall, the results were quite good, considering the complexity of the experiments. Furthermore, several problems with the model were

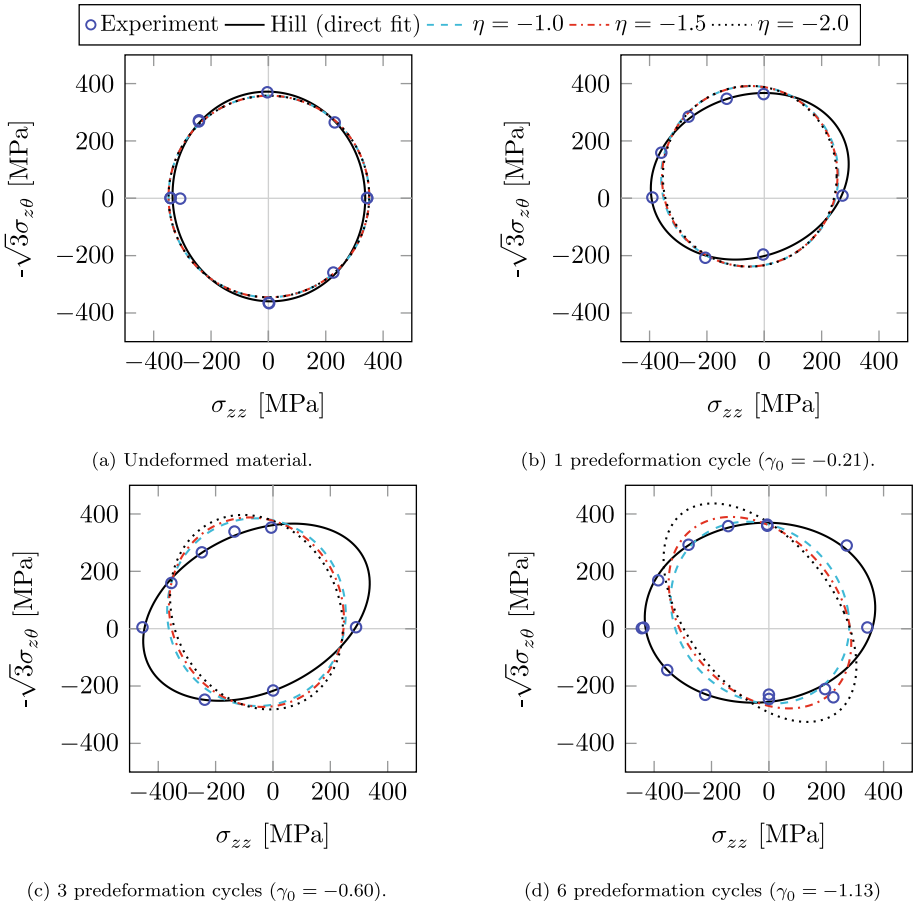

(a) Undeformed material.

(b) 1 predeformation cycle ($\gamma_0 = -0.21$).

(c) 3 predeformation cycles ($\gamma_0 = -0.60$).

(d) 6 predeformation cycles ($\gamma_0 = -1.13$)

Fig. 4. Comparison between experiments from Meyer et al. (2020) and yielding based on Larijani et al. (2013) ($\xi = 1$). The results from the latter are scaled and translated to match the Hill. yield surfaces.

found and discussed. Hence, the model is a good candidate for further improvements.

Several other stress-driven approaches have been proposed in the literature. One increasingly popular class is the Homogeneous Anisotropic Hardening (HAH), proposed by Barlat et al. (2011). In this method, the yield surface translation is modeled via the yield surface distortion. One key issue with this framework is that yielding upon unloading cannot be obtained (i.e. the yield surface must contain the origin). However, this, and additional convergence issues (see e.g. Qin et al., 2017), were solved by Holmedal (2019). We note that there are a lot of different yield criteria that can form the basis for modeling distortional hardening. This choice will have a strong influence on the result, as was shown for the notch deformation in Cazacu et al. (2020). Still, in Meyer et al. (2020), it was shown that, for the same experiments as those considered herein, the simple criterion from Hill (1948), combined with yield surface translation, was accurate.

4. Improved model

We denote the Shi model in Meyer (2020) as the reference model and propose an improved model building upon that model. Two issues with the reference model were discussed in Meyer et al. (2020). First, the yield surface convexity cannot be guaranteed for multiple load paths. As shown in Plesek et al. (2010), it can be very complicated to derive limit cases to ensure convexity. Second, it turned out that the softening in the loading direction could cause a lack of a solution to the local problem. The exact bounds to avoid this could not be determined. Additionally, as discussed in Plesek et al. (2010), the assumption of co-axiality between the current back-stress and the direction of high curvature is questionable. These three concerns are addressed with the improved model proposed herein. We first discuss and motivate the improvements, followed by a complete description of the improved model. The parts of the reference model that are different from the improved model are presented in Appendix D for completeness.

4.1. Motivation of improvements

The first issue discussed in Meyer (2020) was to guarantee the convexity of the yield surface. An interesting solution to this problem exists in many models used to describe higher-order yield functions, such as in Barlat et al. (2005). This approach uses an isotropic and convex yield criterion, but the stress, e.g., $\boldsymbol{\sigma}$, is transformed by a 4th order tensor, $\mathbf{L}$. By using this transformed stress, $\mathbf{L} : \boldsymbol{\sigma}$, the resulting yield criterion is also convex, but not isotropic (as described in Barlat et al., 2005).

The second issue discussed in Meyer (2020) was excessive softening in the loading direction. Consider an effective stress $\sqrt{\boldsymbol{\sigma}^{\text{dev}} : \tilde{\mathbf{C}} : \boldsymbol{\sigma}^{\text{dev}}}$. If $\tilde{\mathbf{C}}$ evolves such that $\boldsymbol{\sigma}^{\text{dev}} : \tilde{\mathbf{C}} : \boldsymbol{\sigma}^{\text{dev}} / [\boldsymbol{\sigma}^{\text{dev}} : \boldsymbol{\sigma}^{\text{dev}}]$ increases, softening occurs (in the absence of other hardening mechanisms). If this evolution is too rapid, no solution for a positive plastic multiplier exists, which was shown in Appendix C.2 in Meyer (2020). The same issue can also occur for purely linear isotropic hardening, setting the isotropic hardening modulus

$H_{\text{iso}} = -3G$, where G is the elastic shear modulus. However, the parameter bounds are not as straightforward for the distortional hardening formulation from e.g. Shi et al. (2014). Therefore, we propose to solve this issue by removing the self-hardening and replacing it with a second isotropic hardening stress. The idea of using multiple isotropic hardening stresses came from Qin et al. (2018). This addition also reduces the model complexity by removing one fourth-order tensor from the material state description.

The results in Fig. 3b showed that the combination of the Masing effect and polarization of dislocations results in a high curvature in the loading direction. This effect has been observed in many experiments (see e.g. Ishikawa and Sasaki, 1988). As mentioned previously, many models include this effect by using the current back-stress as an indicator for the direction of high curvature. To evaluate if it is reasonable to assume such a coupling, a straightforward numerical evaluation is conducted: We consider the crystal plasticity model with 48 slip systems from Meyer (2020), also used in Section 2. The model is available at `https://github.com/KnutAM/MaterialModels`. The material parameters and preloading amount are changed, such that more plasticity occurs when the load is removed. The crystal elastic parameters, $E_{11} = 251$ GPa, $E_{12} = 163.7$ GPa, and $E_{44} = 105.1$ GPa, as well as the over-stress parameters, $t_* = 849$ s and $n = 19.2$, are the same as in Meyer (2020). The initial yield limit is $R_0 = 10$ MPa and the kinematic hardening parameters are $H_{\text{kin}} = 20$ GPa and $Y_{\text{kin}} = 30$ MPa. Remaining parameters are zero. Additionally, using a high number of random orientations (2^{14}) ensured smooth results for small offsets. As in Meyer (2020), all grains are subjected to the same deformation gradient. The plastic work is calculated for each grain individually as

$$w^{\text{p}}(t_1) = \int_{t_0}^{t_1} \boldsymbol{M} : \boldsymbol{L}_{\text{p}} \mathrm{d}t \tag{6}$$

where t_0 is the time when the loading for evaluating the yield surface starts. The Mandel stress, $\boldsymbol{M}$, and the plastic velocity gradient, $\boldsymbol{L}_{\text{p}}$, are defined in Eqs. (21) and (26), respectively. The total plastic work (per volume) is then taken as the average of all grains following the Taylor homogenization scheme. The loading is stress-controlled, reaching a von Mises stress of 100 MPa in 100 s. We have verified that increasing this time to 1000 s has no discernible influence on the response. The results in Fig. 5 show that the direction of high curvature reverses after higher amounts of plasticity during load removal. This is in contrast to the back-stress which is still positive. Based on these results, it is reasonable to model the two effects as de-coupled, as proposed in Feigenbaum and Dafalias (2008). These findings seem to be in line with the conclusions of experimental studies on dislocation tangles (See Hasegawa et al., 1986; Kocks and Mecking, 2003 and references therein). To the authors' knowledge, however, no experimental studies have been conducted to show this effect on macroscopic yield surfaces.

The results in Fig. 5 show substantial differences between the initial yield surface and the first plastic work contour. For such a material response, it is difficult to determine the true yield surface accurately in experiments. Furthermore, a lack of convexity for the first plastic work contours may be observed. It is important to emphasize that the equal plastic work contours are not yield surfaces. I.e., the material state is not the same along an equal plastic work contour, explaining why the non-convexity does not contradict the convex yield potential. This behavior can also occur in experiments, as reported by Yang et al. (2018). Finally, the high curvature in the loading direction is only present for low amounts of plastic deformation in yield detection. Therefore, highly sensitive experiments are required to replicate the results in Fig. 5.

4.2. Complete model formulation

Before describing the model formulation, a brief summary of the notation used is given. Regular parenthesis, (), are used to denote arguments of a function, while square brackets, [], are used to group entities within equations. 2nd order tensors are written in boldface, e.g. $\boldsymbol{a} = a_{ij}\,\underline{\boldsymbol{e}}_i \otimes \underline{\boldsymbol{e}}_j$, while 4th order tensors are written only as capitalized, boldfaced, upright, e.g. $\mathbf{B} = \mathrm{B}_{ijkl}\,\underline{\boldsymbol{e}}_i \otimes \underline{\boldsymbol{e}}_j \otimes \underline{\boldsymbol{e}}_k \otimes \underline{\boldsymbol{e}}_l$. The double contraction between two 2nd order tensors is defined as $\boldsymbol{a} : \boldsymbol{b} = \mathrm{tr}\left(\boldsymbol{a}\boldsymbol{b}^{\text{t}}\right)$, and the quadruple contraction $\mathbf{A} :: \mathbf{B}$, between two 4th order tensors, $\mathbf{A}$ and $\mathbf{B}$, is defined as $\mathrm{A}_{ijkl}\mathrm{B}_{ijkl}$ (in Cartesian orthonormal coordinate systems). $\mathbf{B}^{\text{T}}$ is defined as the major transpose of a 4th order tensor such that $\boldsymbol{a} : \mathbf{B} : \boldsymbol{b} = \boldsymbol{b} : \mathbf{B}^{\text{T}} : \boldsymbol{a}$. The square root of the 2nd basic invariant, $\mathrm{II}_{\boldsymbol{a}}^{1/2}$, of a 2nd order tensor, $\boldsymbol{a}$, is defined as $\mathrm{II}_{\boldsymbol{a}}^{1/2} = \sqrt{\mathrm{tr}(\boldsymbol{a}\boldsymbol{a})}$ and the third principal invariant, $\mathrm{III}_{\boldsymbol{a}}$, as $\mathrm{III}_{\boldsymbol{a}} = \det(\boldsymbol{a})$. Furthermore, $\boldsymbol{a}_{\text{sym}}$ and $\boldsymbol{a}^{\text{dev}}$ denote the symmetric and deviatoric parts of $\boldsymbol{a}$, respectively. Finally, the non-standard open products $\underline{\otimes}$ and $\overline{\otimes}$ are uniquely defined by the following expressions: $[\boldsymbol{a}\underline{\otimes}\boldsymbol{b}] : \boldsymbol{c} = \boldsymbol{a}\boldsymbol{c}^{\text{t}}\boldsymbol{b}^{\text{t}}$ and $[\boldsymbol{a}\overline{\otimes}\boldsymbol{b}] : \boldsymbol{c} = \boldsymbol{a}\boldsymbol{c}\boldsymbol{b}^{\text{t}}$ where $\boldsymbol{a}, \boldsymbol{b}$, and $\boldsymbol{c}$ are second-order tensors.

The finite strain model formulation starts from the multiplicative decomposition of the deformation gradient $\boldsymbol{F} = \boldsymbol{F}_{\text{e}}\boldsymbol{F}_{\text{p}}$ into an elastic, $\boldsymbol{F}_{\text{e}}$, and a plastic, $\boldsymbol{F}_{\text{p}}$, part. The model is formulated on the intermediate configuration, given by the push-forward from the reference configuration using $\boldsymbol{F}_{\text{p}}$. The so-called Mandel stress, $\boldsymbol{M}$, is used in the formulation. It is related to the standard Kirchhoff stress $\boldsymbol{\tau}$ by

$$\boldsymbol{M} = \boldsymbol{F}_{\text{e}}^{\text{t}}\boldsymbol{\tau}\boldsymbol{F}_{\text{e}}^{-\text{t}} \tag{7}$$

4.2.1. Yield formulation

The yield function is formulated as

$$\Phi = f(\boldsymbol{M}_{\text{red}}, \mathbf{C}, \hat{\boldsymbol{r}}) - Y \leqslant 0 \tag{8}$$

The yield function is formulated in terms of quantities settled in the intermediate configuration. Therefore, we require it to be isotropic in its arguments (i.e. be formulated with invariants). The reduced Mandel stress $\boldsymbol{M}_{\text{red}}$ is defined as

$$\boldsymbol{M}_{\text{red}} = \boldsymbol{M}_{\text{red}} - \sum_{i=1}^{N_{\text{back}}} \boldsymbol{M}_{\text{kin},i} \tag{9}$$

$\boldsymbol{M}_{\text{kin},i}$ are the N_{back} back-stresses due to kinematic hardening ($N_{\text{back}} = 2$ in the present paper). These stresses and their evolution are later defined in Eqs. (22) and (27). The use of multiple back-stresses is common in the literature and was first introduced by Chaboche et al. (1979). The effective stress, $f(\boldsymbol{M}_{\text{red}}, \mathbf{C}, \hat{\boldsymbol{r}})$, is additionally dependent on the structure tensor, $\mathbf{C}$, and the curvature tensor, $\hat{\boldsymbol{r}}$, i.e.

$$\begin{aligned} f(\boldsymbol{M}_{\text{red}}, \mathbf{C}, \hat{\boldsymbol{r}}) &= \sqrt{\frac{3}{2}\left[\mathbf{C} : \boldsymbol{M}_{\text{red}}^{\text{dev}}\right]^{\text{t}} : \left[\mathbf{C} : \boldsymbol{M}_{\text{red}}^{\text{dev}}\right]}\sqrt{1 - \boldsymbol{N} : \hat{\boldsymbol{r}}} \\ &= \sqrt{\boldsymbol{M}_{\text{red}}^{\text{dev}} : \hat{\mathbf{C}} : \boldsymbol{M}_{\text{red}}^{\text{dev}}} \end{aligned} \tag{10}$$

where the evolution of $\hat{\boldsymbol{r}}$ is defined by Eqs. (23) and (29). It is uncoupled from the back-stress, which is motivated by the results in Fig. 5. Such uncoupling was first proposed by Feigenbaum and Dafalias (2008). The anisotropy tensor, $\hat{\mathbf{C}}$, can be identified as

$$\hat{\mathbf{C}} = \frac{3}{2}\mathbf{C}^{\text{T}} : [\boldsymbol{I}\underline{\otimes}\boldsymbol{I}] : \mathbf{C}[1 - \boldsymbol{N} : \hat{\boldsymbol{r}}] \tag{11}$$

with $\boldsymbol{I}$ being the 2nd order identity tensor. The loading direction, $\boldsymbol{N}$, is further defined as

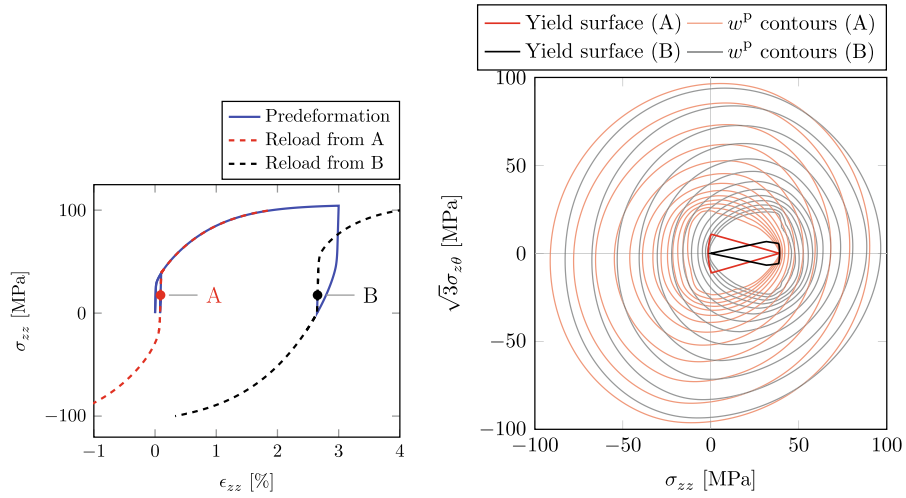

(a) Small (A) and large (B) predeformation, including axial stress-strain curves for uni-axial reloading in tension and compression.

(b) Yield surfaces and logarithmically spaced equal plastic work ($w^{\mathrm{p}} \in [10^{-7}, 10^{-4}]\,\mathrm{mJ/mm^3}$) contours after predeformation A and B.

Fig. 5. Lack of coupling between the direction of high curvature and the current back-stress. Simulated using crystal plasticity with all stress components apart from σ_{zz} and $\sigma_{z\theta} = \sigma_{\theta z}$ being zero.

$$\boldsymbol{N} = \frac{\left[\boldsymbol{M}^{\mathrm{dev}}_{\mathrm{red}}\right]^{\mathrm{t}}}{\mathrm{II}^{1/2}_{\boldsymbol{M}^{\mathrm{dev}}_{\mathrm{red}}}} \tag{12}$$

where we note that $\boldsymbol{N}$ is not necessarily perpendicular to the yield surface. Furthermore, $\mathbf{C}$ is given as a linear combination of the 4th order deviatoric identity tensor, $\mathbf{I}^{\mathrm{dev}} = \boldsymbol{I}\overline{\otimes}\boldsymbol{I} - \boldsymbol{I}\otimes\boldsymbol{I}/3$, and the cross hardening tensor, $\mathbf{C}_{\mathrm{c}}$, specifically

$$\mathbf{C} = \left[[1 - b_{\mathrm{c}}]\mathbf{I}^{\mathrm{dev}} + b_{\mathrm{c}}\mathbf{C}_{\mathrm{c}}\right] \tag{13}$$

where the material parameter b_{c} was introduced.

Isotropic hardening is represented by

$$Y = Y_0 + \sum_{i=1}^{2} Y_{\infty,i}\left[1 - \exp\left(k_{\mathrm{iso},i}\lambda\right)\right], \quad \lambda = \int_0^t \dot{\lambda}\mathrm{d}t \tag{14}$$

where $\dot{\lambda}$ is the plastic multiplier. Y_0 is the initial yield limit, $Y_{\infty,i}$ describe the saturation values for isotropic hardening and $k_{\mathrm{iso},i}$ the corresponding hardening rates.

The gradient of the yield surface, which will be used for the evolution laws, can now be derived as

$$\frac{\partial\Phi}{\partial\boldsymbol{M}} = \frac{1}{2f(\boldsymbol{M}_{\mathrm{red}}, \mathbf{C}, \hat{\boldsymbol{r}})}\left[\hat{\mathbf{C}} : \boldsymbol{M}_{\mathrm{red}} + \boldsymbol{M}_{\mathrm{red}} : \hat{\mathbf{C}} + \frac{f(\boldsymbol{M}_{\mathrm{red}}, \mathbf{C}, \hat{\boldsymbol{r}})^2}{\mathrm{II}^{1/2}_{M^{\mathrm{dev}}_{\mathrm{red}}}[1 - \hat{\boldsymbol{r}} : \boldsymbol{N}]}\left[\hat{\boldsymbol{r}}^{\mathrm{t}} - [\hat{\boldsymbol{r}} : \boldsymbol{N}]\boldsymbol{N}\right]\right] \tag{15}$$

Note that the present model assumes elastic isotropy. Hence, the Mandel stresses are symmetric, and their transpositions do not influence the mechanical response. However, as Sweeney et al. (2013) showed, elastic anisotropy strongly influences damage evolution in ferritic microstructures. So to allow for a straightforward generalization to elastic anisotropy, as in e.g. Bertram and Böhlke (2002), we do not assume a symmetric Mandel stress in the model formulation. The motivation for the transpositions in the yield formulation is given in Appendix B.

4.2.2. Helmholtz free energy

We assume that the Helmholtz free energy, Ψ, is additively decomposed into an elastic part, Ψ_{e}, and inelastic parts corresponding to kinematic hardening, $\Psi_{\mathrm{kin},i}$, cross hardening, Ψ_{c} and distortional hardening, Ψ_{r}, i.e.

$$\Psi = \Psi_{\mathrm{e}}(\boldsymbol{C}_{\mathrm{e}}) + \sum_{i=1}^{N_{\mathrm{back}}}\Psi_{\mathrm{kin},i}(\boldsymbol{c}_{\mathrm{kin},i}) + \Psi_{\mathrm{r}}(\boldsymbol{c}_{\mathrm{r}}) + \Psi_{\mathrm{c}}(\mathbf{A}_{\mathrm{c}}) \tag{16}$$

The elastic energy, Ψ_{e}, follows a standard compressible Neo-Hookean formulation

$$\Psi_{\mathrm{e}} = \frac{G}{2}\left[\mathrm{tr}(\boldsymbol{C}_{\mathrm{e}})\mathrm{III}^{-1/3}_{\boldsymbol{C}_{\mathrm{e}}} - 3\right] + \frac{K}{2}\left[\sqrt{\mathrm{III}_{\boldsymbol{C}_{\mathrm{e}}}} - 1\right]^2 \tag{17}$$

where G is the shear modulus and K is the bulk modulus. The kinematic hardening energies, $\Psi_{\mathrm{kin},i}$, use the same Neo Hookean format, but only for the deviatoric part (following e.g. Wallin et al., 2003),

$$\Psi_{\mathrm{kin},i} = \frac{H_{\mathrm{kin},i}}{2}\left[\mathrm{tr}(\boldsymbol{c}_{\mathrm{kin},i})\mathrm{III}^{-1/3}_{\boldsymbol{c}_{\mathrm{kin},i}} - 3\right] \tag{18}$$

where $H_{\mathrm{kin},i}$ are the kinematic hardening moduli. The directional distortional hardening energy, Ψ_{r}, uses the same Neo-Hookean format as the kinematic hardening,

$$\Psi_{\mathrm{r}} = \frac{H_{\mathrm{r}}}{2}\left[\mathrm{tr}(\boldsymbol{c}_{\mathrm{r}})\mathrm{III}^{-1/3}_{\boldsymbol{c}_{\mathrm{r}}} - 3\right] \tag{19}$$

where H_{r} is a modulus describing how fast the directional distortion evolves. Finally, in analogy to Shi et al. (2014), the cross hardening free energy is introduced as

$$\Psi_{\mathrm{c}} = \frac{c_{\mathrm{c}}}{2}\mathbf{A}^{\mathrm{T}}_{\mathrm{c}} :: \mathbf{A}_{\mathrm{c}} \tag{20}$$

where c_{c} is a material parameter affecting the rate of cross hardening evolution. To the authors' knowledge, Feigenbaum and Dafalias (2007) were the first to introduce such an expression for distortional hardening. In that paper, however, the distortional hardening represented self-hardening (i.e. the yield limit in the loading direction is affected by the evolution of $\mathbf{A}$). Later, Feigenbaum and Dafalias (2014) addressed such distortional hardening for finite plastic strains.

It is noted that the above choices of free energy relate back-stresses and distortional hardening to fictitious deformation gradients. For kinematic hardening, this has been motivated from the microstructure, see e.g. Wallin et al. (2003) and Dettmer and

Reese (2004). Although the motivations are different, Meyer and Ekh (2017) showed that these frameworks are equivalent. In the opinion of the authors, the description with fictitious deformation gradients provides a mathematical framework for hardening contributions by analogy with the framework of material isomorphism as common in plasticity theory. In fact, this framework has proven very efficient in avoiding issues associated with finite simple shear, described in e.g. Ekh (2001). Menzel et al. (2005) extended this approach to include anisotropic damage. Inspired by these previous works, we use the same approach for the directional distortional hardening in Eq. (29) as for the kinematic hardening in Eq. (27).

Based on Ψ, the energetically dual quantities are introduced as

$$\boldsymbol{M} = 2\boldsymbol{C}_\mathrm{e}\frac{\partial \Psi_\mathrm{e}}{\partial \boldsymbol{C}_\mathrm{e}} = G\mathrm{III}_{\boldsymbol{C}_\mathrm{e}}^{-1/3}\boldsymbol{C}_\mathrm{e}^{\mathrm{dev}} + K\left[\mathrm{III}_{\boldsymbol{C}_\mathrm{e}} - \sqrt{\mathrm{III}_{\boldsymbol{C}_\mathrm{e}}}\right]\boldsymbol{I} \tag{21}$$

$$\boldsymbol{M}_{\mathrm{kin},i} = 2\boldsymbol{c}_{\mathrm{kin},i}\frac{\partial \Psi_{\mathrm{kin},i}}{\partial \boldsymbol{c}_{\mathrm{kin},i}} = H_{\mathrm{kin},i}\mathrm{III}_{\boldsymbol{c}_{\mathrm{kin},i}}^{-1/3}\boldsymbol{c}_{\mathrm{kin},i}^{\mathrm{dev}} \tag{22}$$

$$\boldsymbol{r} = 2\boldsymbol{c}_\mathrm{r}\frac{\partial \Psi_\mathrm{r}}{\partial \boldsymbol{c}_\mathrm{r}} = H_\mathrm{r}\mathrm{III}_{\boldsymbol{c}_\mathrm{r}}^{-1/3}\boldsymbol{c}_\mathrm{r}^{\mathrm{dev}} \tag{23}$$

$$\mathbf{C}_\mathrm{c} = -\frac{\partial \Psi_\mathrm{c}}{\partial \mathbf{A}_\mathrm{c}} = -c_\mathrm{c}\mathbf{A}_\mathrm{c}^{\mathrm{T}} \tag{24}$$

where $\boldsymbol{r}$ is related $\hat{\boldsymbol{r}}$ via the material parameter r_{scale}, such that $\boldsymbol{r} = r_{\mathrm{scale}}\hat{\boldsymbol{r}}$. Moreover, the deformations tensors, $\boldsymbol{C}_\mathrm{e}, \boldsymbol{c}_{\mathrm{kin},i}$, and $\boldsymbol{c}_\mathrm{r}$, are defined as

$$\boldsymbol{C}_\mathrm{e} = \boldsymbol{F}_\mathrm{e}^{\mathrm{t}}\boldsymbol{F}_\mathrm{e}, \quad \boldsymbol{c}_{\mathrm{kin},i} = \boldsymbol{F}_{\mathrm{kin},i}^{-\mathrm{t}}\boldsymbol{F}_{\mathrm{kin},i}^{-1}, \quad \boldsymbol{c}_\mathrm{r} = \boldsymbol{F}_\mathrm{r}^{-\mathrm{t}}\boldsymbol{F}_\mathrm{r}^{-1} \tag{25}$$

where the deformation gradients $\boldsymbol{F}_{\mathrm{kin},i}$ and $\boldsymbol{F}_\mathrm{r}$ are state variables along with $\mathbf{A}_\mathrm{c}$ and $\boldsymbol{F}_\mathrm{p}$. All these state variables are established on the same intermediate configuration, which is a common isoclinic configuration, cf. Mandel (1971). Consequently, one can use regular rates for all these variables. The restriction of a common isoclinic configuration can be lifted by introducing different co-rotational rate evolution equations for different variables, following Dafalias (1998). Such an extension is not considered in the present work.

4.2.3. Evolution equations for state variables

We postulate an associative plastic flow

$$\dot{\boldsymbol{F}}_\mathrm{p}\boldsymbol{F}_\mathrm{p}^{-1} =: \boldsymbol{L}_\mathrm{p} = \dot{\lambda}\boldsymbol{v}, \quad \boldsymbol{v} = \frac{\partial \Phi}{\partial \boldsymbol{M}} \tag{26}$$

resulting in an isoclinic intermediate configuration, cf. Mandel (1973) and Dafalias (1998). Therefore, the antisymmetric part of Eq. (26) constitutes the plastic spin constitutive equation (Mandel, 1971; Dafalias, 1985). In the case of isotropic elasticity, and thus a symmetric Mandel stress, the plastic spin is zero and the isoclinic configuration coincides with the so-called spinless intermediate configuration.

The kinematic hardening follows the non-associative evolution law obtained by combining the evolution equations from Frederick and Armstrong (2007) and Burlet and Cailletaud (1986).

$$\dot{\boldsymbol{F}}_{\mathrm{kin},i}\boldsymbol{F}_{\mathrm{kin},i}^{-1} =: \boldsymbol{L}_{\mathrm{kin},i} = \dot{\lambda}\left[-\boldsymbol{v} + \mathrm{II}_{\boldsymbol{v}}^{1/2}\boldsymbol{v}_{\mathrm{kin},i}^{*}\right] \tag{27}$$

$$\boldsymbol{v}_{\mathrm{kin},i}^{*} = \delta\frac{\boldsymbol{M}_{\mathrm{kin},i}^{\mathrm{t}}}{B_{\infty,i}} + [1-\delta]\left[\frac{\boldsymbol{M}_{\mathrm{kin},i} : \hat{\boldsymbol{v}}}{B_{\infty,i}}\right]\hat{\boldsymbol{v}}, \quad \hat{\boldsymbol{v}} = \frac{\boldsymbol{v}}{\mathrm{II}_{\boldsymbol{v}}^{1/2}} \tag{28}$$

where δ is a material parameter controlling the amount of Armstrong-Frederick and Burlet-Cailletaud hardening, while $B_{\infty,i}$ controls the saturation of the effective back-stresses. The non-standard scaling of the kinematic hardening, $\mathrm{II}_{\boldsymbol{v}}^{1/2}$, is introduced following Meyer (2020), inspired by Feigenbaum and Dafalias (2007), to ensure saturation to $B_{\infty,i}$. We note, however, that Dafalias and Feigenbaum (2011) showed that $\delta < 0.5$ can lead to back-stresses outside the desired bounding sphere described by $B_{\infty,i}$, causing kinematic softening contributions for specific load paths. As a better fit is observed for $\delta < 0.5$, this model deficiency is accepted in the present work. We will return to this in the discussion. Finally, the asymmetric (directional) and symmetric distortional hardening are introduced as

$$\dot{\boldsymbol{F}}_\mathrm{r}\boldsymbol{F}_\mathrm{r}^{-1} =: \boldsymbol{L}_\mathrm{r} = \dot{\lambda}\left[-\boldsymbol{N} + \frac{\boldsymbol{r}^{\mathrm{t}}}{r_\infty}\right] \tag{29}$$

and

$$\dot{\mathbf{A}}_\mathrm{c} = \dot{\lambda}d_\mathrm{c}\left[\mathbf{N}_\perp^{\mathrm{T}} :: \mathbf{C}_\mathrm{c}\right]\mathbf{N}_\perp^{\mathrm{T}}, \quad \mathbf{N}_\perp = \mathbf{I}^{\mathrm{dev}} - \boldsymbol{N}^{\mathrm{t}} \otimes \boldsymbol{N} \tag{30}$$

respectively. The initial value of $\mathbf{A}_\mathrm{c}$ is $-\mathbf{I}^{\mathrm{dev}}/c_\mathrm{c}$.

4.2.4. Dissipation inequality

The requirement of positive dissipation is fundamental in material modeling. Dafalias et al. (2002) developed a model with distortional hardening using a 4th order tensor that fulfilled this requirement. For the present model, Clausius-Duhem's reduced dissipation inequality becomes

$$D = \boldsymbol{M} : \boldsymbol{L}_\mathrm{p} + \sum \boldsymbol{M}_{\mathrm{kin},i} : \boldsymbol{L}_{\mathrm{kin},i} + \boldsymbol{r} : \boldsymbol{L}_\mathrm{r} + \mathbf{C}_\mathrm{c} :: \dot{\mathbf{A}}_\mathrm{c} \geqslant 0 \tag{31}$$

Inserting the evolution laws we obtain

$$D/\dot{\lambda} = \boldsymbol{M}_{\mathrm{red}} : \boldsymbol{v} + \sum \boldsymbol{M}_{\mathrm{kin},i} : \boldsymbol{v}_{\mathrm{kin},i}^{*} + \boldsymbol{r} : \left[\boldsymbol{r}^{\mathrm{t}}/r_\infty - \boldsymbol{N}\right] + d_\mathrm{c}\left[\mathbf{C}_\mathrm{c} :: \mathbf{N}_\perp^{\mathrm{T}}\right]^2 \tag{32}$$

The parameter $d_\mathrm{c} > 0$ can be considered a purely thermodynamic parameter. It does not add a degree of freedom to the mechanical response, as the evolution of $\mathbf{C}_\mathrm{c}$ is controlled by the product $c_\mathrm{c}d_\mathrm{c}$, i.e.

$$\dot{\mathbf{C}}_\mathrm{c} = -\dot{\lambda}c_\mathrm{c}d_\mathrm{c}\left[\mathbf{N}_\perp^{\mathrm{T}} :: \mathbf{C}_\mathrm{c}\right]\mathbf{N}_\perp \tag{33}$$

However, d_c is required in the formulation to have correct units. Similarly, the scaled tensor $\hat{\boldsymbol{r}} = \boldsymbol{r}/r_{\mathrm{scale}}$ is used in Eq. (8). The parameter r_{scale} only scales H_r and r_∞ and thus does not add an independent material parameter.

The term $\boldsymbol{M}_{\mathrm{red}} : \boldsymbol{v}$ in Eq. (32) becomes

$$\boldsymbol{M}_{\mathrm{red}} : \boldsymbol{v} = \frac{1}{2f(\boldsymbol{M}_{\mathrm{red}}, \mathbf{C}, \hat{\boldsymbol{r}})}\left[2\boldsymbol{M}_{\mathrm{red}} : \hat{\mathbf{C}} : \boldsymbol{M}_{\mathrm{red}} + \frac{[f(\boldsymbol{M}_{\mathrm{red}}, \mathbf{C}, \hat{\boldsymbol{r}})]^2}{\mathrm{II}_{\boldsymbol{M}_{\mathrm{red}}}^{1/2}[1 - \hat{\boldsymbol{r}} : \boldsymbol{N}]}\underbrace{[\boldsymbol{M}_{\mathrm{red}} : \hat{\boldsymbol{r}}^{\mathrm{t}} - [\hat{\boldsymbol{r}} : \boldsymbol{N}][\boldsymbol{M}_{\mathrm{red}} : \boldsymbol{N}]]}_{=0}\right] \tag{34}$$

$$= f(\boldsymbol{M}_{\mathrm{red}}, \mathbf{C}, \hat{\boldsymbol{r}}) \tag{35}$$

which is strictly positive during plastic loading (it is also remarked that the function f is homogeneous of degree one with respect to $\boldsymbol{M}_{\mathrm{red}}$). Combining Eq. (28) and the term $\sum \boldsymbol{M}_{\mathrm{kin},i} : \boldsymbol{v}_{\mathrm{kin},i}^{*}$, both resulting terms become quadratic multiplied by model parameters. Consequently, these terms are non-negative, provided that $B_{\infty,i}, \delta, [1-\delta] \geqslant 0$. Furthermore, we require that $\mathrm{II}_{\boldsymbol{r}}^{1/2} \leqslant 1$ to avoid taking the square root of a potentially negative number, cf. Eq. (10). Letting $r_{\mathrm{scale}} \to 0$, the influence from $\boldsymbol{r}$ on the dissipation in Eq. (32) vanishes as $\mathrm{II}_{\boldsymbol{r}}^{1/2} \to 0$. Hence, the contribution to the dissipation from the potentially negative term, $\boldsymbol{r} : [\boldsymbol{r}^{\mathrm{t}}/r_\infty - \boldsymbol{N}]$, vanishes. Note that the first term in Eq. (32) is strictly positive. Finally, the last term, $d_\mathrm{c}\left[\mathbf{C}_\mathrm{c} :: \mathbf{N}_\perp^{\mathrm{T}}\right]^2$, is quadratic and, therefore, non-negative for $d_\mathrm{c} \geqslant 0$. In conclusion, the dissipation inequality is fulfilled.

4.2.5. Numerical implementation

The evolution equations for $\boldsymbol{F}_\mathrm{p}, \boldsymbol{F}_{\mathrm{kin},i}$, and $\boldsymbol{F}_\mathrm{r}$ are integrated using the standard exponential map,

$$\boldsymbol{F}_{\mathrm{p}} = \exp(\Delta\lambda \boldsymbol{v})\ {}^{n}\boldsymbol{F}_{\mathrm{p}} \tag{36}$$

$$\boldsymbol{F}_{\mathrm{kin},i} = \exp\left(\Delta\lambda\left[-\boldsymbol{v} + \mathrm{II}_{\boldsymbol{v}}^{1/2}\boldsymbol{v}^{*}_{\mathrm{kin},i}\right]\right)\ {}^{n}\boldsymbol{F}_{\mathrm{p}} \tag{37}$$

$$\boldsymbol{F}_{\mathrm{r}} = \exp\left(-\Delta\lambda\left[\boldsymbol{N} - \boldsymbol{r}^{\mathrm{t}}/r_{\infty}\right]\right)\ {}^{n}\boldsymbol{F}_{\mathrm{r}} \tag{38}$$

where the notation ${}^{n}\bullet$ indicates the value of $\bullet$ in the previous time step. For readability, we neglect the notation ${}^{n+1}\bullet$ for the value in the current time step. Furthermore, $\Delta\lambda = \dot{\lambda}[t_{n+1} - t_n]$. Finally, following Bartels and Mosler (2017), we adopt the exponential map for $\mathbf{C}_{\mathrm{c}}$, which reduces to a scalar exponential, specifically

$$\mathbf{C}_{\mathrm{c}} = {}^{n}\mathbf{C}_{\mathrm{c}} + \frac{1}{7}\left[\exp\left(-7c_{\mathrm{c}}d_{\mathrm{c}}\Delta\lambda\right) - 1\right]\left[{}^{n}\mathbf{C}_{\mathrm{c}} :: \mathbf{N}_{\perp}^{\mathrm{T}}\right]\mathbf{N}_{\perp} \tag{39}$$

4.2.6. Material parameters

To summarize the proposed material model, the material parameters are described in Table 1. Parameters marked with (*) do not add independent mechanical modeling parameters but ensure that the units in the model are correct. However, they do influence the dissipation, which is important in a thermomechanical simulation. In this work we set $r_{\mathrm{scale}} = d_{\mathrm{c}} = 1$ MPa.

5. Comparison to experiments

In this section, we compare the improved model to experimental results. These experiments are presented briefly below; the complete description exists in Meyer et al. (2020). After that, we give a brief overview of the simulation methodology. In the present work, we improve the analysis of the experiments in conjunction with the material model framework. This analysis leads to the approximation of effective plastic strains and is presented in Subsection 5.3. Using this approximation, we present the material parameter identification scheme in Subsection 5.4. Finally, in Subsection 5.5, we present the ability of the improved material model to fit and predict the experimental results.

5.1. Overview of experiments

The experiments used in the present study are from Meyer et al. (2020). In that study, cylindrical test bars, such as the bar in Fig. 6, were subjected to torsion during axial compressive loads. The material in the 14 mm diameter gauge section sustains large shear deformations as shown in Fig. 6b. The predeformation was conducted in steps of 90° rotation with nominal axial stress −600 MPa.

After the predeformation, the test bars were re-machined to form thin-walled tubular test bars. The inside hole was gun-drilled to 12 mm, and the outside turned and polished to 14 mm. These predeformed, thin-walled, test bars were loaded in different directions in the $\epsilon_{zz} - \epsilon_{z\theta}$ plane. The response in different directions, both without predeformation and after 1, 3, and 6 predeformation steps, was evaluated.

5.2. Overview of simulation methodology

In Meyer et al. (2019), a simulation methodology for Axial-Torsion-Pressure (ATP) simulation was developed together with the open-source material model fitting tool, `matmodfit` (Meyer, 2019). The ATP simulation methodology was extended to include re-machining in Meyer (2020). This enhancement allowed the experiments in Meyer et al. (2020) to be simulated efficiently.

The ATP simulation framework is a 1-dimensional finite element simulation, which allows non-linear variation of stresses, strains, and material state along the radial direction. The following kinematic constraints are assumed:

Table 1
Description of material parameters.

Parameter	Unit	Description
G	[MPa]	Shear modulus
K	[MPa]	Bulk modulus
Y_0	[MPa]	Initial yield limit
$k_{\mathrm{iso},i}$	[–]	Isotropic hardening rate
$Y_{\infty,i}$	[MPa]	Isotropic saturation stress
$H_{\mathrm{kin},i}$	[MPa]	Kinematic hardening modulus
$B_{\infty,i}$	[MPa]	Kinematic saturation stress
δ	[–]	AF vs BC kinematic hardening
H_{r}	[MPa]	Hardening modulus for $\boldsymbol{r}$
r_{∞}	[MPa]	Saturation value for $\boldsymbol{r}$
r_{scale} (*)	[MPa]	Unit scaling of $\boldsymbol{r}$
c_{c}	[MPa^{-1}]	Hardening rate for $\mathbf{C}_{\mathrm{c}}$
b_{c}	[–]	Influence from $\mathbf{C}_{\mathrm{c}}$
d_{c} (*)	[MPa]	Thermodynamic parameter for $\mathbf{C}_{\mathrm{c}}$

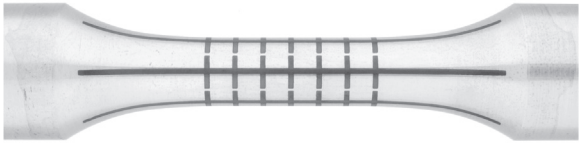

(a) Undeformed specimen.

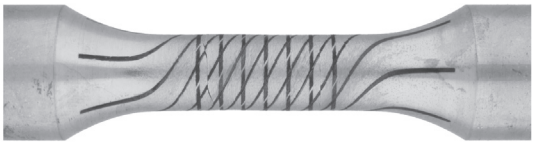

(b) Deformed specimen.

Fig. 6. Specimen with orthogonal laser mesh before and after predeformation from Meyer et al. (2018b) (Reprinted w.ith permission).

$$\begin{array}{lll} & \frac{\partial\theta}{\partial R} = 0 & \frac{\partial z}{\partial R} = 0 \\ \frac{\partial r}{\partial\Theta} = 0 & \frac{\partial\theta}{\partial\Theta} = 1 & \frac{\partial z}{\partial\Theta} = 0 \\ \frac{\partial r}{\partial Z} = 0 & \frac{\partial\theta}{\partial Z} = \frac{\phi}{H} & \frac{\partial u_z}{\partial Z} = \frac{\Delta z}{H} \end{array} \tag{40}$$

where R, Θ, Z are the undeformed coordinates and r, θ, z are the deformed coordinates. These kinematic constraints, along with the coordinate system and the radial discretization, are shown in Fig. 7. There, the degrees of freedom $u_{r,1}, \ldots, u_{r,N}, \phi, \Delta z$ are introduced, where N is the number of nodes. The associated external loads $p_{\mathrm{i}}, p_{\mathrm{o}}, T_z, F_z$ are also shown. For further details, please see Meyer et al. (2019).

5.3. Approximation of effective plastic strains

The experiments in Meyer et al. (2020) were conducted in two stages. First, solid test bars were predeformed under combined torsion and axial compression. These test bars were then re-machined into thin-walled tubular test bars. The mechanical behavior of these bars was then evaluated in the second step, with particular emphasis on the yield surface. In Meyer (2020), the experimental and numerical results were analyzed equally, treating both as experimental data. However, in the present study, we seek to provide a more accurate description of the numerical result, using the state described by the material model's state variables (more specifically $\boldsymbol{F}_{\mathrm{p}}$). However, to do this properly, the different configurations in Fig. 8 must be analyzed carefully.

The real configurations are those that are observable. Ω_0 is the initial (or undeformed) configuration, and Ω is the current configuration (during the second part of the experiment as described

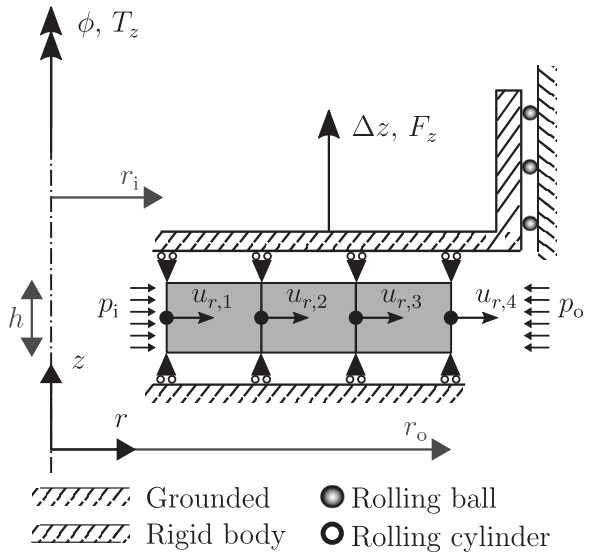

Fig. 7. Kinematic assumptions and degrees of freedom for ATP simulations from Meyer et al. (2019) (Reprinted with permission).

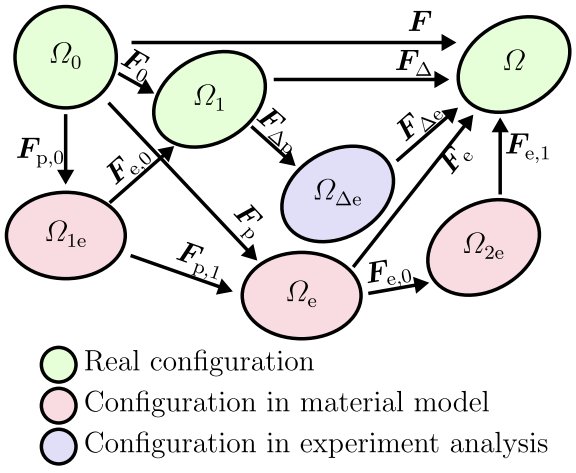

Fig. 8. The different configurations and deformation gradients in the experimental results.

above). The configuration Ω_1 is the deformed configuration after the predeformation and re-machining step, obtained via the deformation gradient $\boldsymbol{F}_0$. Following the standard multiplicative decomposition of the deformation gradient, $\boldsymbol{F} = \boldsymbol{F}_\mathrm{e}\boldsymbol{F}_\mathrm{p}$, the intermediate configuration, Ω_e, is introduced in the material model. After part one of the experiment, this split becomes $\boldsymbol{F}_0 = \boldsymbol{F}_{\mathrm{e},0}\boldsymbol{F}_{\mathrm{p},0}$, resulting in the intermediate configuration, $\Omega_{1\mathrm{e}}$. Furthermore, we have the total deformation gradient $\boldsymbol{F} = \boldsymbol{F}_{\mathrm{e},1}\boldsymbol{F}_{\mathrm{e},0}\boldsymbol{F}_{\mathrm{p},1}\boldsymbol{F}_{\mathrm{p},0}$, where $\boldsymbol{F}_{\mathrm{e},1}$ and $\boldsymbol{F}_{\mathrm{p},1}$ evolve in the second part of the experiment. Thus, it is natural to introduce another intermediate configuration, $\Omega_{2\mathrm{e}}$, to indicate the split of the elastic deformation gradient $\boldsymbol{F}_\mathrm{e} = \boldsymbol{F}_{\mathrm{e},1}\boldsymbol{F}_{\mathrm{e},0}$. When analyzing the experiments, however, the configuration Ω_1 is treated as the initial configuration. Hence, when calculating the split between plastic and elastic deformations, another intermediate configuration, $\Omega_{\Delta\mathrm{e}}$, appears. It does not exist in the material model. This subsection aims to relate the effective plastic strain in the experiments (related to $\boldsymbol{F}_{\Delta\mathrm{p},1}$) and in the simulations (related to $\boldsymbol{F}_{\mathrm{p},1}$).

Due to the thin-walled geometry, we assume that the stress at Ω_1 is zero. As the stress depends on the related elastic right or left Cauchy-Green deformation tensors, $\boldsymbol{F}_{\mathrm{e},0} = \boldsymbol{Q}$ is a proper rotation tensor (i.e., $\boldsymbol{Q}\boldsymbol{Q}^\mathrm{t} = \boldsymbol{I}$). $\boldsymbol{F}_{\mathrm{e},0}$ will be denoted $\boldsymbol{Q}$ in the following derivation, to emphasize this property. We then have that

$$\boldsymbol{F}_{\Delta\mathrm{e}}\boldsymbol{F}_{\Delta\mathrm{p}} = \boldsymbol{F}_{\mathrm{e},1}\boldsymbol{Q}\boldsymbol{F}_{\mathrm{p},1}\boldsymbol{Q}^\mathrm{t} \tag{41}$$

Considering that the elastic strains are small, we can, as a reasonable approximation, use any suitable elastic constitutive relation. Choosing a linear elastic relation based on the Almansi strain, $\boldsymbol{e}$, and the 4th order elasticity tensor, $\mathbf{E}$, we have the Kirchhoff stress on the current configuration, Ω, namely

$$\mathbf{E} : \boldsymbol{e}_{\Delta\mathrm{e}} \approx \boldsymbol{\tau} \approx \mathbf{E} : \boldsymbol{e}_\mathrm{e}, \quad \boldsymbol{e}_\bullet = \frac{1}{2}\left[\boldsymbol{I} - \boldsymbol{F}_\bullet^{-\mathrm{t}}\boldsymbol{F}_\bullet^{-1}\right] \tag{42}$$

From this argument, we obtain that $\boldsymbol{e}_{\Delta\mathrm{e}} \approx \boldsymbol{e}_\mathrm{e}$. Using that $\boldsymbol{Q}\boldsymbol{Q}^\mathrm{t} = \boldsymbol{I}$, we furthermore see that $\boldsymbol{e}_\mathrm{e} \approx \boldsymbol{e}_{\mathrm{e},1}$. As the deformation in the second part of the experiment is small we may neglect the rotation of $\boldsymbol{F}_{\Delta\mathrm{e}}$ and $\boldsymbol{F}_{\mathrm{e},1}$. Hence, we may assume that $\boldsymbol{F}_{\Delta\mathrm{e}} \approx \boldsymbol{F}_{\mathrm{e},1}$, which, together with Eq. (41), results in

$$\boldsymbol{F}_{\Delta\mathrm{p}} \approx \boldsymbol{Q}\boldsymbol{F}_{\mathrm{p},1}\boldsymbol{Q}^\mathrm{t} \tag{43}$$

It is now of interest to consider if we can have the same effective strain measure in both the simulation and the experiments. Following the above derivation, it is natural to consider the Almansi strains in the continuation. As the strains in the second part are small, we consider the linearization of the Almansi strain for the experiments with

$$\dot{\boldsymbol{e}}_\Delta = -\frac{1}{2}\left[\dot{\boldsymbol{F}}_{\Delta\mathrm{e}}^{-\mathrm{t}}\left[\boldsymbol{I} - 2\boldsymbol{e}_{\Delta\mathrm{p}}\right]\boldsymbol{F}_{\Delta\mathrm{e}}^{-1} + \boldsymbol{F}_{\Delta\mathrm{e}}^{-\mathrm{t}}\left[\boldsymbol{I} - 2\boldsymbol{e}_{\Delta\mathrm{p}}\right]\dot{\boldsymbol{F}}_{\Delta\mathrm{e}}^{-\mathrm{t}} - 2\boldsymbol{F}_{\Delta\mathrm{e}}^{-\mathrm{t}}\dot{\boldsymbol{e}}_{\Delta\mathrm{p}}\boldsymbol{F}_{\Delta\mathrm{e}}^{-1}\right] \tag{44}$$

so that $\boldsymbol{e}_{\Delta\mathrm{p}} \ll \boldsymbol{I}$ and $\boldsymbol{F}_{\Delta\mathrm{e}} \approx \boldsymbol{I}$ result in

$$\boldsymbol{e}_\Delta \approx \boldsymbol{e}_{\Delta\mathrm{e}} + \boldsymbol{e}_{\Delta\mathrm{p}} \tag{45}$$

Introducing the von Mises effective Almansi plastic strain, $e_{\Delta\mathrm{p}}^{\mathrm{vM}}$, we obtain

$$e_{\Delta\mathrm{p}}^{\mathrm{vM}} = \sqrt{\frac{2}{3}\boldsymbol{e}_{\Delta\mathrm{p}}^{\mathrm{dev}} : \boldsymbol{e}_{\Delta\mathrm{p}}^{\mathrm{dev}}} = \sqrt{\frac{2}{3}\left[\boldsymbol{e}_{\Delta\mathrm{p}} : \boldsymbol{e}_{\Delta\mathrm{p}} - \frac{1}{3}\left[\mathrm{tr}(\boldsymbol{e}_{\Delta\mathrm{p}})\right]^2\right]} \tag{46}$$

Moreover, inserting the definition of $\boldsymbol{e}_{\Delta\mathrm{p}}$ in Eq. (46) yields

$$e_{\Delta\mathrm{p}}^{\mathrm{vM}} = \sqrt{\frac{1}{6}}\sqrt{\left[\boldsymbol{F}_{\Delta\mathrm{p}}^{-\mathrm{t}}\boldsymbol{F}_{\Delta\mathrm{p}}^{-1}\right] : \left[\boldsymbol{F}_{\Delta\mathrm{p}}^{-\mathrm{t}}\boldsymbol{F}_{\Delta\mathrm{p}}^{-1}\right] - \frac{1}{3}\left[\mathrm{tr}\left(\boldsymbol{F}_{\Delta\mathrm{p}}^{-\mathrm{t}}\boldsymbol{F}_{\Delta\mathrm{p}}^{-1}\right)\right]^2} \tag{47}$$

Using the approximation in Eq. (43), we can see, without further approximations, that

$$\left[\boldsymbol{F}_{\Delta\mathrm{p}}^{-\mathrm{t}}\boldsymbol{F}_{\Delta\mathrm{p}}^{-1}\right] : \left[\boldsymbol{F}_{\Delta\mathrm{p}}^{-\mathrm{t}}\boldsymbol{F}_{\Delta\mathrm{p}}^{-1}\right] \approx \left[\boldsymbol{F}_{\mathrm{p},1}^{-\mathrm{t}}\boldsymbol{F}_{\mathrm{p},1}^{-1}\right] : \left[\boldsymbol{F}_{\mathrm{p},1}^{-\mathrm{t}}\boldsymbol{F}_{\mathrm{p},1}^{-1}\right] \tag{48}$$

$$\mathrm{tr}\left(\boldsymbol{F}_{\Delta\mathrm{p}}^{-\mathrm{t}}\boldsymbol{F}_{\Delta\mathrm{p}}^{-1}\right) \approx \mathrm{tr}\left(\boldsymbol{F}_{\mathrm{p},1}^{-\mathrm{t}}\boldsymbol{F}_{\mathrm{p},1}^{-1}\right) \tag{49}$$

Hence, the effective plastic Almansi von Mises strain is approximately the same when calculated using $\boldsymbol{F}_{\Delta\mathrm{p}}$ and $\boldsymbol{F}_{\mathrm{p},1}$, i.e. $e^{\mathrm{vM}}(\boldsymbol{F}_{\Delta\mathrm{p}}) \approx e^{\mathrm{vM}}(\boldsymbol{F}_{\mathrm{p},1})$. Note that this result would not be obtained if, e.g., the small strain tensor $\boldsymbol{\epsilon}_{\mathrm{p},1} = \left[\boldsymbol{F}_{\mathrm{p},1}\right]_{\mathrm{sym}} - \boldsymbol{I}$ would have been used instead of the Almansi strain.

Following the methodology in, e.g., Meyer et al. (2020), the elastic compliance tensor, $\mathbf{E}^{-1}$, herein related to the Almansi strains, is obtained by a least-square fitting approach for the elastic data points from the experiments. The elastic range is determined by finding the yield points when using an isotropic elasticity tensor. Young's modulus is set to 212 GPa and the shear modulus to 80.5 GPa, and a small plastic offset is used. Then, half the von Mises stress at the yield point is taken as maximum elastic stress for that particular loading direction. Given the compliance tensor, $\mathbf{E}^{-1}$, the elastic Almansi strains, $\boldsymbol{e}_{\Delta\mathrm{e}}$, may be calculated, i.e.

$$\boldsymbol{e}_{\Delta\mathrm{e}} = \mathbf{E}^{-1} : \boldsymbol{\tau} \tag{50}$$

where all components in $\boldsymbol{\tau}$ are zero, except τ_{zz} and $\tau_{z\theta} = \tau_{\theta z}$. Only the corresponding components in $\boldsymbol{e}_{\Delta e}$ can be calculated. In the experiment, $[\boldsymbol{F}_\Delta]_{zz}$ and $[\boldsymbol{F}_\Delta]_{\theta z}$ are measured. Based on the kinematic assumptions in Eq. (40), all shear components, except $[\boldsymbol{F}_\Delta]_{\theta z}$ may be assumed to be zero. This gives after some manipulations

$$[\boldsymbol{e}_\Delta] = \frac{1}{2}[\boldsymbol{I}] - \frac{1}{2}\begin{bmatrix} \frac{1}{[\boldsymbol{F}_\Delta]_{rr}^2} & 0 & 0 \\ 0 & \frac{1}{[\boldsymbol{F}_\Delta]_{\theta\theta}^2} & -\frac{[\boldsymbol{F}_\Delta]_{\theta z}}{[\boldsymbol{F}_\Delta]_{\theta\theta}^2[\boldsymbol{F}_\Delta]_{zz}} \\ 0 & -\frac{[\boldsymbol{F}_\Delta]_{\theta z}}{[\boldsymbol{F}_\Delta]_{\theta\theta}^2[\boldsymbol{F}_\Delta]_{zz}} & \frac{1}{[\boldsymbol{F}_\Delta]_{zz}^2} + \frac{[\boldsymbol{F}_\Delta]_{\theta z}^2}{[\boldsymbol{F}_\Delta]_{\theta\theta}^2[\boldsymbol{F}_\Delta]_{zz}^2} \end{bmatrix} \tag{51}$$

$$\approx \begin{bmatrix} [\boldsymbol{F}_\Delta]_{rr} & 0 & 0 \\ 0 & [\boldsymbol{F}_\Delta]_{\theta\theta} & 0.5[\boldsymbol{F}_\Delta]_{\theta z} \\ 0 & 0.5[\boldsymbol{F}_\Delta]_{\theta z} & [\boldsymbol{F}_\Delta]_{zz} \end{bmatrix} - [\boldsymbol{I}] \tag{52}$$

hence, $[\boldsymbol{e}_{\Delta p}]_{zz}$ and $[\boldsymbol{e}_{\Delta p}]_{z\theta} = [\boldsymbol{e}_{\Delta p}]_{\theta z}$ can be calculated using Eq. (45). By assuming a transversely isotropic elastic behavior w.r.t. the r-axis, we may assume that all shear components of $\boldsymbol{e}_{\Delta e}$, except $[\boldsymbol{e}_{\Delta e}]_{z\theta} = [\boldsymbol{e}_{\Delta e}]_{\theta z}$, are zero. Thus, the same holds for $\boldsymbol{e}_{\Delta p}$. Finally, we assume that $[\boldsymbol{e}_{\Delta p}]_{rr} \approx [\boldsymbol{e}_{\Delta p}]_{\theta\theta}$ such that $\mathrm{tr}(\boldsymbol{e}_{\Delta p}) = 0$ (deviatoric plastic strains).[1] This gives the effective plastic strain

$$e_{\Delta p}^{vM} = \sqrt{[\boldsymbol{e}_{\Delta p}]_{zz}^2 + \frac{4}{3}[\boldsymbol{e}_{\Delta p}]_{\theta z}^2} \tag{53}$$

If the approximation of small strains in the experiments is used in Eq. (52), the standard small strain tensor, $\boldsymbol{\epsilon}_\Delta = [\boldsymbol{F}_\Delta]_{sym} - \boldsymbol{I}$, is obtained. We use this approximation as the strains in the second part of the experiment are small, and consequently, the rotation in $\boldsymbol{F}_\Delta$ is small. However, the Almansi plastic strain for the simulation must be calculated using $\boldsymbol{F}_{p,1}$. Otherwise, the rotation in $\boldsymbol{Q}$ will affect the results. We have verified that the approximations described above are reasonable by using synthetically generated experimental data, based on the proposed material model.

Finally, the yield point can be determined by interpolating between the stresses when the plastic strain is just below and just above a given offset strain.

5.4. Material parameter identification

To identify the material parameters, we use numerical optimization, minimizing the difference between the simulated and experimental results. The experiments are simulated following the methodology developed in Meyer (2020). A key in material parameter identification is the calculation of the difference between experiments and simulations. This calculation is described in Subsection 5.4.1 below, followed by a description of the optimization algorithm and the determination of parameter bounds.

5.4.1. Objective function

The most straight forward method to calculate the simulation error is to consider the stress and strain difference to the experiments. However, we know from previous experience (Meyer, 2020) that this method is not suitable when attempting to describe anisotropic yield surfaces. Therefore, we adopt a similar method as in Meyer (2020), but with some key improvements. The overall concept is the same; the error in strains and torque during the predeformation gives one contribution, and the error in the yield surfaces give the other contribution. The yield surfaces are considered for two levels of plastic deformation contours. Many models and model evaluations consider the effect of strain-path changes, see e.g. Teodosiu and Hu (1995), Wang et al. (2008), Qin et al. (2019). By considering the stress state at multiple plastic deformation levels, we effectively take the stress-strain curve into account in the objective function. In this work, we improve the yield surface detection and also include the stress direction at yielding. These changes are motivated below.

An issue with using the plastic work as a description for the amount of plasticity at yield point detection is that the plastic work is affected by a translated yield surface. In the extreme case with a yield surface that excludes the origin, the plastic work may be negative upon yielding. We, therefore, propose to use effective Almansi plastic strains instead. How these strains are approximated in the experiments was described above in Section 5.3.

In order to better describe the material state at the yield point, we also include a description of the flow direction at the detected yield point. Most plasticity models assume associative plastic flow. This assumption implies that the plastic flow direction is normal to the yield surface. However, the exact start of plastic deformations cannot be detected in experiments. Therefore, the measured yield surface is not the true yield surface. Fig. 5b illustrates this well, where only the contours at which some plasticity already has occurred can be detected. Thus, assuming that the plastic flow is normal to a yield contour is not the same as assuming associative plastic flow. However, in this study, we are comparing the experiments with a numerical model. The model assumes associative plastic flow. In this case, it is possible to compare the direction of plastic flow between the experiment and the simulation. The experiments were strain-controlled, and we can calculate the flow direction from the stress path. However, as shown in Appendix C, the flow direction has a larger experimental scatter than the stress path. Therefore, we use the difference in stress direction, following Appendix C, as part of the objective function. The flow direction is an important characteristic of the material behavior. For example, Cazacu and Rodríguez-Martínez (2019) showed that it can explain the development of shear bands. For sheet metals, the Lankford coefficient R (see ISO, 2020), is often studied. Considering the instantaneous Lankford coefficient, r (cf. Barlat et al., 2005), we have (assuming small strains), that

$$r = \frac{[\dot{\boldsymbol{e}}_{\Delta p}]_{yy}}{[\dot{\boldsymbol{e}}_{\Delta p}]_{zz}} = -\frac{[\dot{\boldsymbol{e}}_{\Delta p}]_{yy}}{[\dot{\boldsymbol{e}}_{\Delta p}]_{xx} + [\dot{\boldsymbol{e}}_{\Delta p}]_{yy}} \tag{54}$$

where x is the longitudinal, y the transverse, and z the thickness direction and we use the rates of the plastic Almansi strain defined in Eq. (45). The last equality in Eq. (54) assumes plastic incompressibility. The instantaneous Lankford coefficient is thus a measure of the flow direction. By including the stress path in our objective function, the instantaneous Lankford coefficient is also considered when evaluating the material models.

In summary, the predeformation error, E_{pdef}, is described in Meyer (2020) and the yield point error, E_y, is described in Appendix C. The total simulation error is given as the sum of these and constitutes the objective function used in the minimization procedures. We do not fit the yield behavior after all six predeformation steps. This behavior is used to evaluate the models' predictive abilities.

5.4.2. Numerical optimization scheme

The optimization consists of five steps. First, we generate 500 initial guesses via a Latin Hypercube sampling. The subsequent steps use the 100 guesses that produce the lowest objective function. These steps use the Simplex algorithm from Nelder and Mead (1965) to minimize the objective function. The initial size of the simplex is 30% of the parameter space for the first step, and 10% for the three subsequent steps.

[1] The assumption $[\boldsymbol{e}_{\Delta p}]_{rr} \approx [\boldsymbol{e}_{\Delta p}]_{\theta\theta}$ is equivalent to assuming a Lankford coefficient, $R = 1$. If, instead, $R = 0.5$ or $R = 2$, the maximum relative error of the plastic strain is 1.8%, which shows that the approximation is reasonable.

A key input for the parameter identification is the parameter bounds. They affect both the initial guesses and limit the parameter values that the optimization algorithm can attempt. We considered the resulting parameter values for the 10 optimization runs producing the lowest objective function value. If a parameter value was too close to any of its parameter bounds, we adjusted that bound and re-ran the parameter identification.

5.5. Results

The ability of three different models to fit and predict the experimental results are described in this section. The "reference model" is the Shi model from Meyer (2020), which is a modified version of the model in Shi et al. (2014). The equations for this model are given in Appendix D. Additionally, two variants of the improved model are evaluated. One with and one without the directional distortion introduced by $\boldsymbol{r}$, denoted $H_r \neq 0$ and $H_r = 0$, respectively.

Table 2 describes the result of the parameter identification. The reference model and the improved model with $H_r = 0$ have equally many parameters. From the objective function values in Table 2, it is clear that the improved model can fit the experiments better. Allowing $H_r \neq 0$ further improves the fit. However, this model is more complex, and there is an increased parameter and error variation for different start guesses.

Most parameters are very similar between the two variants of the improved model. Still, when $H_r \neq 0$ several of the best 10 results have a pure Armstrong-Frederick type of kinematic hardening ($\delta \approx 1$). The parameters for $H_r \neq 0$ giving the lowest objective function value, shown in Table 2, also have much more Armstrong-Frederick type of kinematic hardening compared to when $H_r = 0$. Additionally, the cross-hardening rate, c_c, is very different. We had to increase the upper parameter bound for this parameter several times. However, the change in the objective function was small ($7 \cdot 10^{-5}$ for a 10-fold increase).

The parameter values for the reference model are similar to those in Meyer (2020), except for c_L. However, following the discussion regarding c_c above, this may be reasonable as c_L and c_c both control the cross hardening. Overall, the low variation in both error and parameter values, indicate that the optimization strategy has successfully identified good parameter values.

Fig. 9 shows the experimental and simulated results for the predeformation, with axis quantities defined in Fig. 7. In Fig. 10a, the rotation and force in the experiment are shown as functions of time. The predeformation level is described by the shear strain due to the predeformation, $\gamma_0 = \phi_z r/H$, where ϕ_z and H are defined in Fig. 7. $r \approx 6.5$ mm is the radius in the middle of the wall of the thin-walled test bars. All models describe the experimental result rather well. The reference model does not capture the initial axial deformation as accurately as the other models but is slightly more accurate at larger rotations. The improved model with $H_r = 0$ shows a too low torque towards the end. However, the hardening during each predeformation step is closer to the experimental values. Fig. 9d shows that all models yield a similar width of the hysteresis loop, which is narrower than the experimental results. It is also noted that the reference model is closer to the experimental results. This is related to the higher torque resulting in more rotation during the load removal.

Fig. 10 shows the ability of each model to fit and predict the yield behavior. The models' responses, calculated for 72 different loading directions, are shown with the radial grey stress paths. Circumferential grey lines show the yield contours for 16 logarithmically spaced effective plastic strain offsets. The smallest strain is 0.001%, and the largest is 1.0%. The red lines show the models' yield contours for effective strains of 0.01% and 0.2%, for which the associated yield points are part of the objective function. Blue circles show the experimental yield points at these strain levels and blue lines the experimental stress path between these points. Hence, a good fit is indicated by blue circles on the red contours and blue lines that align with the radial grey lines.

When inspecting Fig. 10a–c carefully, a lack of symmetry about the vertical axis may be observed, both in the numerical and experimental results. This is due to the Swift effect, see Swift (1947).[2] In the simulation, both the hyperelastic law and the plastic evolution contribute to the Swift effect. Due to the rather small incremental deformations during yield surface detection, the elastic response is important for the results in Fig. 10a–c. The present model does not capture the cyclic Swift effect well. Wallin and Ristinmaa (2005) showed that adding a non-zero constitutive spin (cf. Dafalias, 1998) affects the monotonic Swift effect. Böhlke et al. (2003) developed a phenomenological model with anisotropic elastic stiffness and non-zero constitutive spin, which qualitatively captured the cyclic Swift effect behavior. While the Swift effect is not a focus of the present work, it should be investigated further in future works.

After one predeformation step, $\gamma_0 = -0.21$, all models show a distorted yield surface. The experimental points are captured rather well, even though the shape predicted by the reference and improved models are different. Still, the yield point accuracy, and even more so the stress paths, are better described by the improved models. Similar trends are seen after three predeformation steps, $\gamma_0 = -0.60$. At this point, the non-elliptical shape possible when $H_r \neq 0$ is becoming apparent.

After six predeformation steps, $\gamma_0 = -1.13$, the yield behavior is not part of the objective function. Hence, these results are predicted. Neither of the models can predict the experimental results reasonably well.

To further examine how well the different models capture the material response, Fig. 11 shows the loading in pure tension/compression and shear. The response for the virgin material (Fig. 11a and 11b) is quite different for the reference model compared to the response predicted by the improved models. The experimental results are also more accurately captured by the improved models. After predeformation, the reference model and the other models produce more similar responses. The experimental material response is also captured rather accurately, even though the reference model results deviate more than those from the improved models.

6. Discussion

In Section 2, we concluded that a model for evolving plastic anisotropy should consider three different effects. These were based on simple numerical examples, highlighting the deformation processes that occur in the microstructure of pearlitic steels. In Section 3, we decided that a stress-driven approach seemed more suitable for an accurate and efficient description of evolving anisotropy. The improved model suggested in Section 4 can capture all three effects:

1. The distortion-free yield surface translation due to the Masing effect. It is captured using advanced kinematic hardening that combines the Armstrong-Frederick and Burlet-Cailletaud evolution laws.
2. The asymmetric distortion, due to polarization of dislocations, can be described by the evolution of the curvature tensor $\boldsymbol{r}$ when $H_r \neq 0$.
3. The symmetric distortion of the yield surface is described by the evolution of the cross-hardening tensor, $\mathbf{C}_c$.

[2] The torsional direction has been reversed compared to previous publications to comply with the coordinate system defined in Fig. 7.

Table 2
Optimization results. The variation, denoted by "±", of the values is the standard deviation of the 10 results with the lowest error.

Model	$H_r = 0$	$H_r \neq 0$	reference model	Unit
Error	1.23 ± 0.001	1.05 ± 0.017	1.69 ± 0.001	%
Y_0	352 ± 6	360 ± 7	320 ± 1	MPa
$k_{iso,1}$	904 ± 228	1156 ± 347	–	–
$H_{iso,1}$	–	–	29.3 ± 0.4	GPa
$Y_{\infty,1}$	-321 ± 12	-325 ± 19	1424 ± 10	MPa
$k_{iso,2}$	16.7 ± 0.6	20.6 ± 1.2	–	–
$Y_{\infty,2}$	320 ± 19	296 ± 18	–	MPa
δ	0.582 ± 0.021	0.831 ± 0.089	0.127 ± 0.003	–
$H_{kin,1}$	153 ± 1	171 ± 15	98.5 ± 0.3	GPa
$B_{\infty,1}$	386 ± 3	360 ± 17	419 ± 2	MPa
$H_{kin,2}$	3.25 ± 0.20	5.31 ± 1.8	2.74 ± 0.04	GPa
$B_{\infty,2}$	309 ± 2	284 ± 11	379 ± 1	MPa
c_c	60.6 ± 20.2	5.56 ± 3.07	–	kPa^{-1}
b_c	-0.369 ± 0.007	-0.416 ± 0.022	–	–
H_r	–	0.899 ± 0.224	–	MPa
r_∞	–	0.918 ± 0.133	–	MPa
b_D	–	–	-30.0 ± 0.04	–
b_L	–	–	-7.46 ± 0.19	–
c_D	–	–	30.0 ± 0.05	–
c_L	–	–	905 ± 237	10^3

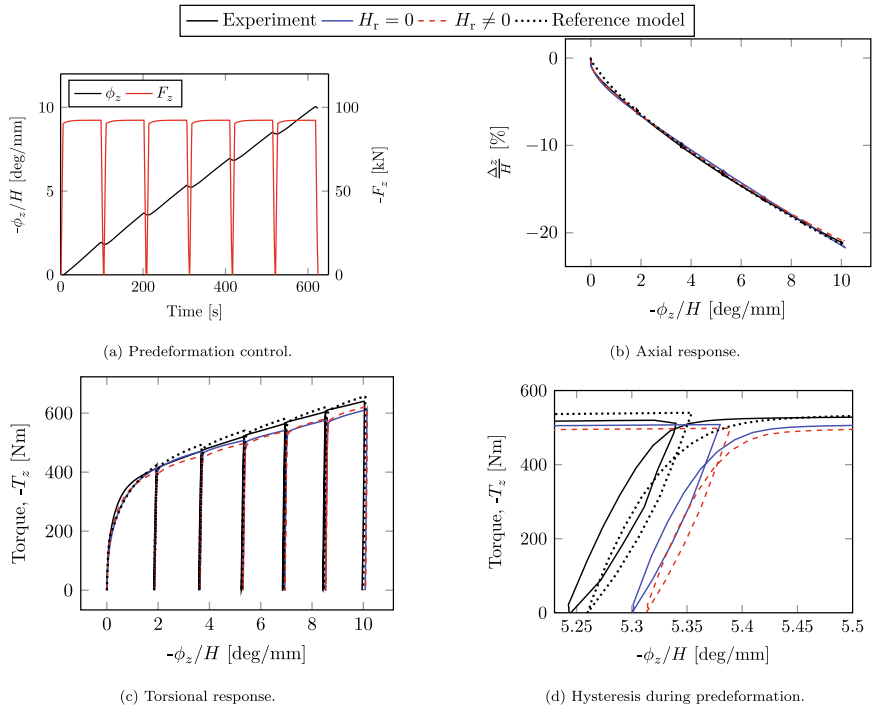

(a) Predeformation control.

(b) Axial response.

(c) Torsional response.

(d) Hysteresis during predeformation.

Fig. 9. Response for predeformation of solid test bars.

The combination of Armstrong-Frederick and Burlet-Cailletaud type of kinematic hardening proved crucial to capture the predeformation response in Meyer et al. (2018a). Without this combination, it was not possible to simultaneously capture the axial and torsional response. That study employed material models with isotropic yield surfaces. For the same experiments as in the present study, the combination significantly improved the present reference model (Shi model in Meyer, 2020). In the present work, the improved model with $H_r = 0$ could also fit the experimental results much better with this combination.

However, for $H_r \neq 0$, many of the best results (i.e. lowest objective function value) had an almost pure Armstrong-Frederick type of kinematic hardening. This observation is particularly interesting given the issues with the Burlet-Cailletaud modification when $\delta < 0.5$. However, this result alone cannot determine whether the introduction of a yield surface curvature tensor $\boldsymbol{r}$ can replace the more advanced kinematic hardening law. More studies, tailored to investigate this particular effect, such as in Feigenbaum et al. (2012), must be conducted.

The decoupling between the direction of high curvature and the current back-stress was motivated in Section 4 by using crystal plasticity. The simplistic Taylor homogenization was used. Additionally, as shown by Pham et al. (2017), the cross-hardening description can strongly influence the anisotropy in crystal plasticity simulations. Consequently, there are many uncertainties related to these simulation results. However, the main phenomenon remains: the current yield surface center and the direction of high curvature were decoupled. We, therefore, conclude

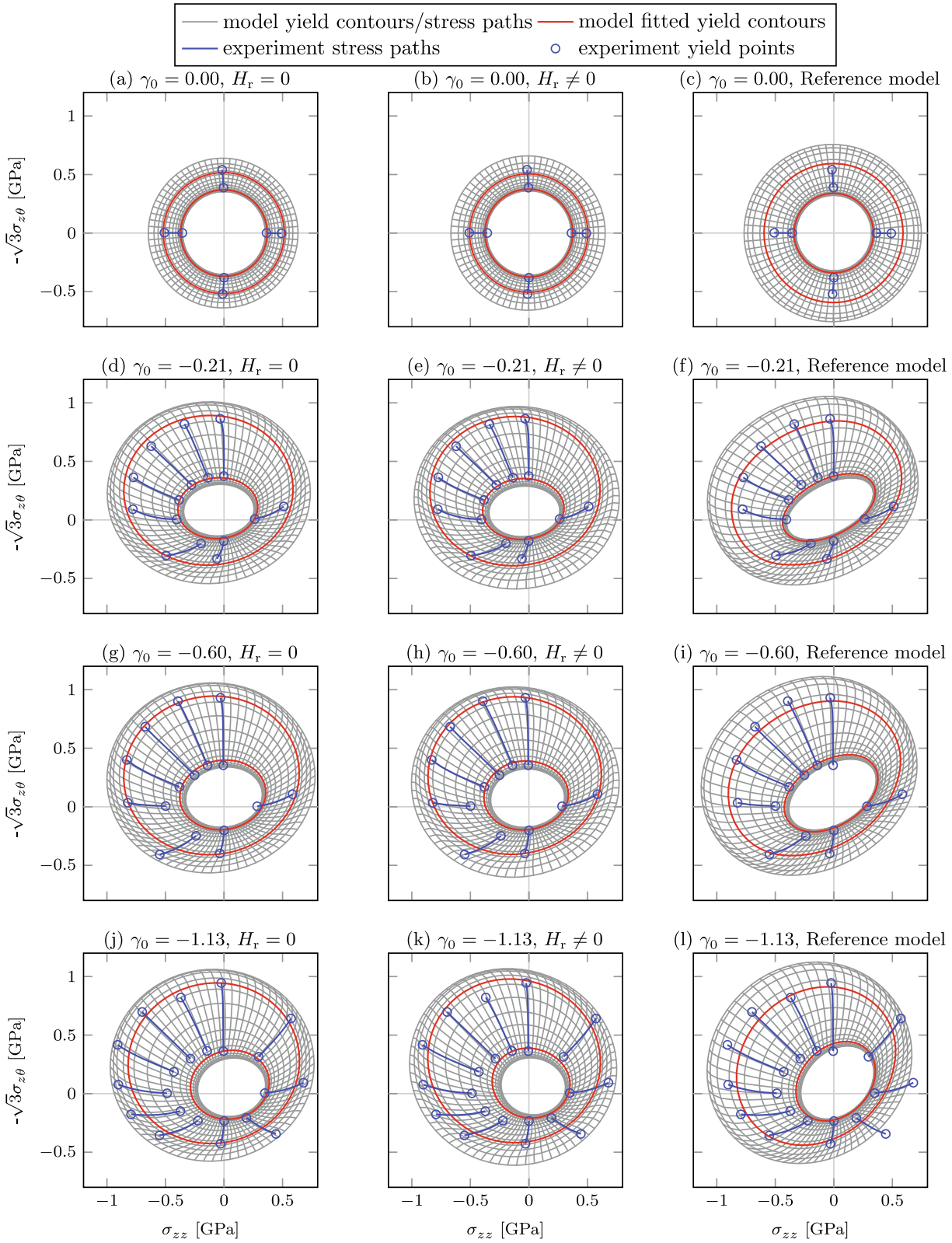

Fig. 10. The ability of each model to fit and predict the yield behavior at different predeformation levels. The level is indicated by the predeformation shear strain γ_0.

that this is not a reasonable modeling assumption. Even so, this conclusion should be strengthened by future experimental results.

An important aspect when considering the high curvature in the loading direction is its importance on the overall material response. As was seen in Fig. 5, the non-ellipticity decreases rapidly with offset strain. Hence, the influence of the high curvature effect in practical applications might be limited. Interesting examples include spring-back in sheet-metal applications or stresses and strains in rolling contact fatigue simulations. However, to investigate this effect, the model must be calibrated to experi-

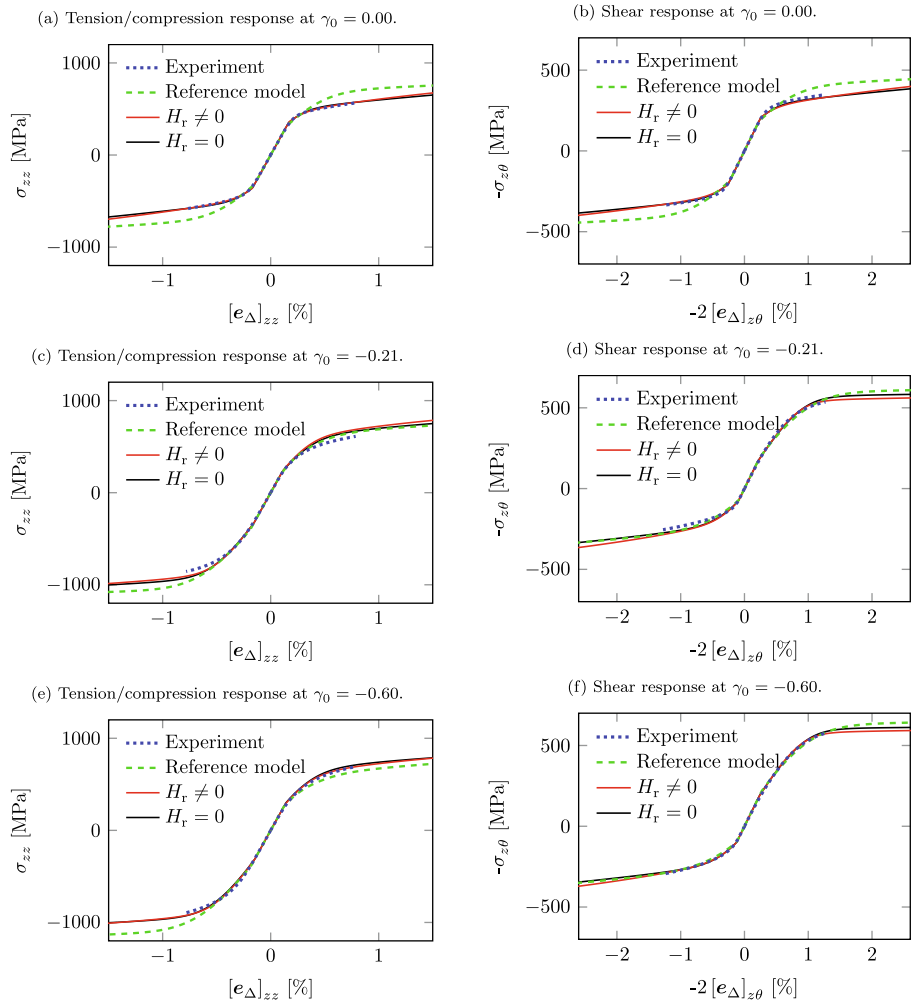

Fig. 11. Stress-strain curves for loading in pure tension/compression and shear after different predeformation levels. Note that each figure describes two experiments, both starting at the origin.

ments where this phenomenon is identifiable. The experimental results in Meyer et al. (2020) do not exhibit such behavior. Consequently, the calibrated response for $H_r \neq 0$ does not seem to capture the high curvature seen in many experimental results. The purpose of this addition is to include a short-term memory of the previous loading direction. On the contrary, the best fit to the experimental data gives a slow evolution of $\boldsymbol{r}$. After $\gamma_0 = -0.21, \mathrm{II}_{\boldsymbol{r}}^{1/2} = 0.10$, increasing via 0.24 at $\gamma_0 = -0.60$ to 0.39 at $\gamma_0 = -1.13$. While it is clear that the addition of the high curvature does improve the ability of the model to fit the results, it is also clear that it does not improve the predictive ability. We propose that this distortion should be calibrated via tailored experiments in the future.

A symmetric distortion was assumed to be due to the reorientation of the substructure in Section 2. However, in stress-driven models, including the improved model described herein, no such coupling exists. The lack of coupling to the substructure evolution is clear as the cross hardening is independent of whether the loading direction $\boldsymbol{N}$ is reversed or not. That is, $\mathbf{N}_\perp = \mathbf{I}^{\mathrm{dev}} - \boldsymbol{N}^{\mathrm{t}} \otimes \boldsymbol{N} = \mathbf{I}^{\mathrm{dev}} - [-\boldsymbol{N}^{\mathrm{t}}] \otimes [-\boldsymbol{N}]$. By comparing the cross hardening between cyclic and monotonic loading, the validity of such a modeling assumption can be evaluated. We propose to conduct such an experiment in future works.

Despite the decoupling with the substructure, the improved model shows a substantial improvement over the previous model. The guaranteed convexity and simplified description of the self-hardening significantly improved the numerical stability. Furthermore, precise parameter bounds simplified the parameter identification. Especially the stress paths were much better predicted, indicating that this is a promising improvement for stress-driven models. However, there was no definite improvement in predictive ability for additional predeformation. In particular, as previously discussed, when $H_r \neq 0$, the yield surface distortion was over-predicted. The validation experiments were extrapolations of the calibration experiments. This setup makes it difficult to give accurate predictions as compared to using less predeformation in the validation set. Finally, only two points on the stress-strain curves where included in the objective function. Even so, the full curves where accurately predicted by the modified models.

A final note on the two improvements to the objective function compared to Meyer (2020), is warranted. The first improvement was to use the approximations following the analysis in Subsection 5.3 to identify yielding in the numerical results. This methodology is more robust as compared to fitting the elastic behavior for each parameter set. For some parameter values during the identification procedure, very unusual material behavior may occur. For these corner cases, the yield point identification procedure may not produce correct results. Hence, we found that the process was improved by directly analyzing the plastic deformation gradient from the model. The second improvement was to include the stress

direction at the yield point in the objective function. In Appendix C, we showed that this is more accurate than using the plastic strain direction. However, we still account for that information indirectly. By including this information in the objective function, we were able to capture the material behavior better while still ensuring an accurate fit to the yield points.

7. Concluding remarks

Departing from simple models of the microstructure, we have evaluated different approaches to capture the evolving plastic anisotropy in metals. We first assessed the use of strain-driven models for a pearlitic steel. The results show that the reorientation of cementite lamellas alone cannot describe the evolution of anisotropy. Furthermore, we show that the evolution laws for strain-driven approaches become computationally expensive if high accuracy is maintained. From a review of different models, we then concluded that the stress-driven method is more suitable.

We proposed an improved stress-driven model that guarantees yield surface convexity and is thermodynamically consistent. Compared to previous models, it significantly improved the fit of the experimental behavior in Meyer et al. (2020), without increasing the complexity. Still, to answer many open questions, specific experiments are required in the future. In particular, the predictive ability of the model is not entirely satisfactory.

In addition to the proposed model, we derived an approximate plastic strain offset, considering finite pre-straining. This approximation made it possible to use the plastic deformation gradient (state variable) to calculate the yield contours from the model. We also included the stress evolution direction at the point of yielding, and explained why the normality rule should not be applied directly to experimentally determined yield contours. These additions, affecting the objective function, resulted in a more stable parameter identification scheme.

Declaration of Competing Interest

The authors declare that they have no known competing financial interests or personal relationships that could have appeared to influence the work reported in this paper.

Acknowledgments

This work is part of the activities within the CHARMEC Centre of Excellence at Chalmers University of Technology. Parts of the study have been funded within the European Union's Horizon 2020 research and innovation programme in the project In2Track2 under grant agreement No. 826255. The majority of the simulations were performed on resources at Chalmers Centre for Computational Science and Engineering (C3SE) provided by the Swedish National Infrastructure for Computing (SNIC). Partial financial support has been provided by Deutsche Forschungsgemeinschaft (DFG, German Research Foundation), Project-ID 278868966 - TRR188, which is gratefully acknowledged. Furthermore, the use of AceGen (Korelc, 2002) has been very effective in speeding up the implementation of the material models.

Appendix A. Structure evolution

Following Larijani et al. (2013) we define an effective stress due to the evolution of cementite lamellas (cl), characterized by their normal vector $\underline{\boldsymbol{n}}$, of the form

$$\tau_{\mathrm{cl}} = \sqrt{\boldsymbol{\tau}^{\mathrm{t}} : \mathbf{C}_{\mathrm{cl}} : \boldsymbol{\tau}} \tag{55}$$

$$\mathbf{C}_{\mathrm{cl}} = 5[\boldsymbol{a} \underline{\otimes} \boldsymbol{I} - \mathbf{B}] \tag{56}$$

$$\langle \bullet \rangle = \int_{\mathrm{sphere}} p(\underline{\boldsymbol{n}}) \bullet \mathrm{d}A \tag{57}$$

$$\boldsymbol{a} = \langle \underline{\boldsymbol{n}} \otimes \underline{\boldsymbol{n}} \rangle \quad \mathbf{B} = \langle \underline{\boldsymbol{n}} \otimes \underline{\boldsymbol{n}} \otimes \underline{\boldsymbol{n}} \otimes \underline{\boldsymbol{n}} \rangle \tag{58}$$

The yield formulation, and in particular the homogenization $\langle \bullet \rangle$, can be interpreted in two different, but still equivalent, ways. First, the average distribution of the current cementite orientation can be considered. Each orientation $\underline{\boldsymbol{n}}$ is then a function of the deformation history and the orientation distribution function (odf), $p(\underline{\boldsymbol{n}}) = 1/4\pi$. The alternative interpretation is to consider the integral over uniformly distributed directions (which are not affected by the deformation), but where the odf, $p(\underline{\boldsymbol{n}})$, evolves as a function of the deformation history.

If areal-affine reorientation is considered, the orientation $\underline{\boldsymbol{n}}$ of a lamella with initial orientation $\underline{\boldsymbol{n}}_0$ is given as

$$\underline{\boldsymbol{n}} = \frac{\boldsymbol{F}^{-\mathrm{t}} \underline{\boldsymbol{n}}_0}{\sqrt{[\boldsymbol{F}^{-\mathrm{t}} \underline{\boldsymbol{n}}_0] \cdot [\boldsymbol{F}^{-\mathrm{t}} \underline{\boldsymbol{n}}_0]}} \tag{59}$$

By taking the time derivative of this expression, the following evolution law for $\underline{\boldsymbol{n}}$ is obtained after some manipulations, specifically

$$\dot{\underline{\boldsymbol{n}}} = \boldsymbol{W} \underline{\boldsymbol{n}} - [\boldsymbol{D} \underline{\boldsymbol{n}} - [\underline{\boldsymbol{n}} \boldsymbol{D} \underline{\boldsymbol{n}}] \underline{\boldsymbol{n}}] \tag{60}$$

which is equivalent to Eq. (5) with $\eta = -1$.

From the two interpretations of the averaging in Eq. (58), there are two possible ways to model the evolution. The first considers the evolution of a discrete set of initial directions $\underline{\boldsymbol{n}}_{0,i}$, which transform to $\underline{\boldsymbol{n}}_i$ according to Eq. (59). These transformed directions are then numerically integrated over the unit sphere, following Menzel and Waffenschmidt (2009)

$$\boldsymbol{a} \approx \sum_{i=1}^{N} w_i \, \underline{\boldsymbol{n}}_i \otimes \underline{\boldsymbol{n}}_i, \quad \mathbf{B} \approx \sum_{i=1}^{N} w_i \, \underline{\boldsymbol{n}}_i \otimes \underline{\boldsymbol{n}}_i \otimes \underline{\boldsymbol{n}}_i \otimes \underline{\boldsymbol{n}}_i \tag{61}$$

where w_i is the weight factor for each direction $\underline{\boldsymbol{n}}_{0,i}$.

The second approach considers the evolution of the structure tensors $\boldsymbol{a}$ and $\mathbf{B}$ directly, see e.g., Menzel et al. (2008). This evolution was derived from the general evolution law,

$$\dot{\underline{\boldsymbol{n}}} = \boldsymbol{W} \underline{\boldsymbol{n}} + \eta [\boldsymbol{D} \underline{\boldsymbol{n}} - [\underline{\boldsymbol{n}} \boldsymbol{D} \underline{\boldsymbol{n}}] \underline{\boldsymbol{n}}] - D_{\mathrm{r}} \frac{1}{p(\underline{\boldsymbol{n}})} \nabla p \tag{62}$$

by Advani and Tucker (1987), i.e.

$$\dot{\boldsymbol{a}} = [\boldsymbol{W}\boldsymbol{a} - \boldsymbol{a}\boldsymbol{W}] + \eta [\boldsymbol{D}\boldsymbol{a} + \boldsymbol{a}\boldsymbol{D} - 2\mathbf{B} : \boldsymbol{D}] + 2 D_{\mathrm{r}} [\boldsymbol{I} - 3\boldsymbol{a}] \tag{63}$$

The reorientation factor η controls the type of evolution of the direction vectors, as in Eq. (5). For the fluid problems discussed in the Advani and Tucker (1987), the rotary diffusivity, D_{r}, can be important. However, in the plastic flow studied in this work, we will assume $D_{\mathrm{r}} = 0$. This assumption implies that the evolution of a lamella is independent of the current distribution of lamella orientations. For this case, the evolution of the 4th order structure tensor $\mathbf{B}$, following Altan et al. (1990) and Jack and Smith (2006), becomes

$$\begin{aligned} \dot{\mathrm{B}}_{ijkl} = & \left[W_{im} \mathrm{B}_{mjkl} + W_{jm} \mathrm{B}_{imkl} + W_{km} \mathrm{B}_{ijml} + W_{lm} \mathrm{B}_{ijkm} \right] \\ & + \eta \left[D_{im} \mathrm{B}_{mjkl} + D_{jm} \mathrm{B}_{imkl} + D_{km} \mathrm{B}_{ijml} + D_{lm} \mathrm{B}_{ijkm} - 4 \mathcal{B}_{ijklmn} D_{mn} \right] \end{aligned} \tag{64}$$

where the 6th order tensor $\boldsymbol{\mathcal{B}}$ is introduced as

$$\boldsymbol{\mathcal{B}} = \langle \underline{\boldsymbol{n}} \otimes \underline{\boldsymbol{n}} \otimes \underline{\boldsymbol{n}} \otimes \underline{\boldsymbol{n}} \otimes \underline{\boldsymbol{n}} \otimes \underline{\boldsymbol{n}} \rangle \tag{65}$$

The evolution of this tensor would include a tensor with an even higher order. Each new tensor requires a higher order tension in the evolution equation. Hence, the evolution cannot be calculated exactly. Advani and Tucker (1987) use so-called closure approximations to obtain an approximate evolution for **B**. We will now compare the accuracy of using such closure approximations with the accuracy of different numerical integration schemes.

We can use a direct closure approximation for **B** and use this in the yield criterion (as done in Johansson and Ekh, 2006). Advani and Tucker (1990) present a hybrid closure, combining a linear and quadratic closure. For **B**, these approximations are

$$\mathbf{B}^{\text{lin}} = -\frac{1}{35}[\boldsymbol{I}\otimes\boldsymbol{I}+\boldsymbol{I}\overline{\otimes}\boldsymbol{I}+\boldsymbol{I}\underline{\otimes}\boldsymbol{I}]+\frac{1}{7}[\boldsymbol{a}\otimes\boldsymbol{I}+\boldsymbol{a}\overline{\otimes}\boldsymbol{I}+\boldsymbol{a}\underline{\otimes}\boldsymbol{I}+\boldsymbol{I}\otimes\boldsymbol{a}+\boldsymbol{I}\overline{\otimes}\boldsymbol{a}+\boldsymbol{I}\underline{\otimes}\boldsymbol{a}] \tag{66}$$

$$\mathbf{B}^{\text{quad}} = \boldsymbol{a}\otimes\boldsymbol{a} \tag{67}$$

$$\mathbf{B}^{\text{hyb}} = [1-f_{\text{q}}]\mathbf{B}^{\text{lin}}+f_{\text{q}}\mathbf{B}^{\text{quad}},\ f_{\text{q}} = 1-27\det(\boldsymbol{a}) \tag{68}$$

Alternatively, we can keep **B** as a state variable and use the closure approximation only for $\mathcal{B}$ in the evolution equation for **B**. These closure approximations are

$$\begin{aligned}\mathcal{B}^{\text{lin}}_{ijklmn} = \ & \tfrac{1}{693}\left[\delta_{ij}\delta_{kl}\delta_{mn}+\delta_{ij}\delta_{km}\delta_{ln}+\cdots(15\text{ terms})\right] \\ & -\tfrac{1}{99}\left[a_{ij}\delta_{kl}\delta_{mn}+a_{ij}\delta_{km}\delta_{ln}+\cdots(45\text{ terms})\right] \\ & +\tfrac{1}{11}\left[\mathrm{B}_{ijkl}\delta_{mn}+\mathrm{B}_{ijkm}\delta_{ln}+\cdots(15\text{ terms})\right]\end{aligned} \tag{69}$$

$$\mathcal{B}^{\text{quad}} = \mathbf{B}\otimes\boldsymbol{a} \tag{70}$$

$$\mathcal{B}^{\text{hyb}} = \left[1-f_{\text{q}}\right]\mathcal{B}^{\text{lin}}+f_{\text{q}}\mathcal{B}^{\text{quad}} \tag{71}$$

Fig. 12 shows the resulting yield surfaces after two different predeformation load steps. The initial yield surface is shown as a comparison. The reference solution is obtained by numerically integrating 10^5 randomly oriented directions (convergence was checked against 10^6 directions). For the tensile preloading in Fig. 12a, the 2×33 formula by Bažant and Oh (1986) is closest to the reference solution. However, for the shear predeformation in Fig. 12b the 2×21 formula is performing best. Due to this surprising result, a test in which the chosen direction vectors in the integration formula was rotated $\pi/10$ radians around the y-axis was performed. The results show that the rotation results in significantly different evolution of the yield surface. A small deviation should be expected. However, the large differences in Fig. 12 show a strong non-objectivity. This effect is reduced with higher-order integration schemes, but that results in higher computational cost.

When a closure approximation is used to determine **B**, the yield surface distortion is under-predicted. When **B** is evolved, and $\mathcal{B}$ is approximated, more accurate results are obtained. However, after shear loading, Fig. 12b show that this higher-order closure does not produce accurate results. The number of terms in Eq. (69) results in a scheme that is computationally much more expensive than the evaluated numerical integration formulas. However, the advantage of using the direct evolution of the orientation tensors is the objectivity. The lack of this feature is a crucial deficiency with the numerical integration schemes.

Appendix B. Motivation of transpositions

The Mandel stress, $\boldsymbol{M} = \boldsymbol{F}_{\text{e}}^{\text{t}}\boldsymbol{\tau}\boldsymbol{F}_{\text{e}}^{-\text{t}}$, is a mixed tensor (co- and contravariant), i.e. $\boldsymbol{M} = M_i^j\tilde{\underline{\boldsymbol{G}}}^i\otimes\tilde{\underline{\boldsymbol{G}}}_j$, where $\tilde{\underline{\boldsymbol{G}}}^i$ and $\tilde{\underline{\boldsymbol{G}}}_j$ are the co- and contravariant basis on the intermediate configuration. We remark that, from a geometrical point of view, the introduced transposition formally corresponds to the dual quantity. Hence, $\boldsymbol{M}-\boldsymbol{M}^{\text{t}}$ is not a valid operation. Secondly, a pressure independent yield criterion is typically formulated based on the 2nd invariant of the stress on the current configuration. In this model based on the symmetric Kirchhoff stress, $\boldsymbol{\tau}$, we note that

$$\boldsymbol{\tau}:\boldsymbol{\tau} = \boldsymbol{\tau}^{\text{t}}:\boldsymbol{\tau} = \boldsymbol{M}^{\text{t}}:\boldsymbol{M} \neq \boldsymbol{M}:\boldsymbol{M} \tag{72}$$

for a non-symmetric Mandel stress.

$\mathbf{C}_{\text{c}}$ is double contracted with $\boldsymbol{M}_{\text{red}} = \boldsymbol{M}-\sum\boldsymbol{M}_{\text{kin},i}$ in Eq. (10). Considering now the evolution of $\mathbf{C}_{\text{c}}$ using backward Euler we have

$$\mathbf{C}_{\text{c}} = {}^{\text{n}}\mathbf{C}_{\text{c}}+\Delta\lambda\left[\mathbf{C}_{\text{c}}::\mathbf{N}_{\perp}^{*}\right]\left[\mathbf{I}^{\text{dev}}-\boldsymbol{N}^{\text{t}}\otimes\boldsymbol{N}\right],\quad \boldsymbol{N} = \left[\boldsymbol{M}_{\text{red}}^{\text{t}}\right]^{\text{dev}}/\text{II}_{\boldsymbol{M}_{\text{red}}^{\text{dev}}}^{1/2} \tag{73}$$

$$\mathbf{C}_{\text{c}}:\boldsymbol{M}_{\text{red}} = {}^{\text{n}}\mathbf{C}_{\text{c}}:\boldsymbol{M}_{\text{red}}+\Delta\lambda\left[\mathbf{C}_{\text{c}}::\mathbf{N}_{\perp}^{*}\right]\left[\boldsymbol{M}_{\text{red}}^{\text{dev}}-\boldsymbol{N}^{\text{t}}[\boldsymbol{N}:\boldsymbol{M}_{\text{red}}]\right] \tag{74}$$

where we have yet to decide if $\mathbf{N}_{\perp}^{*}$ is $\mathbf{N}_{\perp}$ or $\mathbf{N}_{\perp}^{\text{T}}$. For consistency, we see that we should subtract $\boldsymbol{N}^{\text{t}}$ from $\boldsymbol{M}_{\text{red}}^{\text{dev}}$ and not $\boldsymbol{N}$, motivating the transpose in $\mathbf{N}_{\perp} = \mathbf{I}^{\text{dev}}-\boldsymbol{N}^{\text{t}}\otimes\boldsymbol{N}$. Now, let's consider the quadruple contraction $\mathbf{C}_{\text{c}}::\mathbf{N}_{\perp}^{*}$ in the same fashion. In particular, $\left[\boldsymbol{N}^{\text{t}}\otimes\boldsymbol{N}\right]::\mathbf{N}_{\perp}^{*}$ is interesting. Choosing $\mathbf{N}_{\perp}^{*} = \mathbf{I}^{\text{dev}}-\boldsymbol{N}\otimes\boldsymbol{N}^{\text{t}} = \mathbf{N}_{\perp}^{T}$ works out such that

$$\left[\boldsymbol{N}^{\text{t}}\otimes\boldsymbol{N}\right]::\left[\mathbf{I}^{\text{dev}}-\boldsymbol{N}\otimes\boldsymbol{N}^{\text{t}}\right] = 1-\left[\boldsymbol{N}^{\text{t}}:\boldsymbol{N}\right]\left[\boldsymbol{N}:\boldsymbol{N}^{\text{t}}\right] \tag{75}$$

Appendix C. Flow direction

The data from each experiment includes the time history of the axial stress, $\sigma = [\boldsymbol{\sigma}]_{zz}$, the shear stress, $\tau = [\boldsymbol{\sigma}]_{z\theta}$, the axial strain, $\epsilon = [\boldsymbol{e}_{\Delta}]_{zz}$, and the shear strain, $\gamma = 2[\boldsymbol{e}_{\Delta}]_{\theta z}$. We only consider the second part of the experiment (the reloading), and in this part, the strains are small following the analysis in Section 5.3. In the

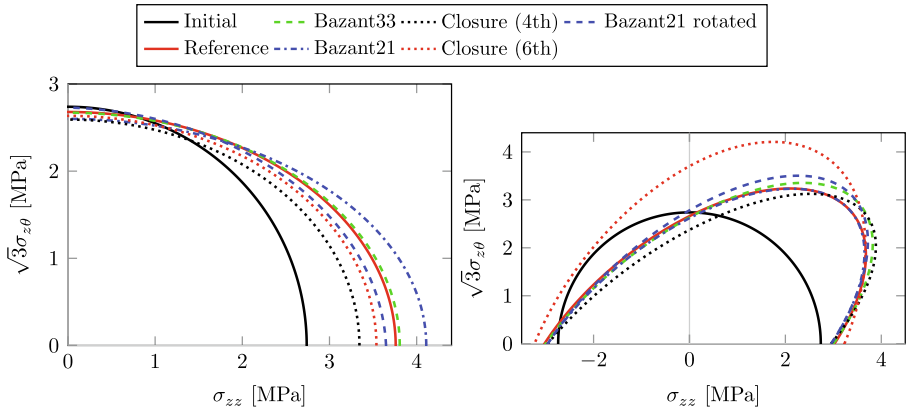

(a) Isochoric tension, $F_{zz} = 2.0$, $F_{\theta\theta} = F_{rr} = 1/\sqrt{2}$ (b) Simple shear, $F_{z\theta} = 2.0$

Fig. 12. Resulting yield surfaces for different reorientation modeling approaches after simple predeformations. All stress components, except $\sigma_{z\theta} = \sigma_{\theta z}$ and σ_{zz}, are zero.

following analysis we, therefore, assume small strains for simplicity. The two strain components are controlled, while the stress components represent the material response. A yield point, $\boldsymbol{\sigma}_y$, given by the yield stress components σ_y and τ_y is determined according to the method in Section 5.3. In addition to this point itself, the current evolution directions may be investigated. The evolution direction, $\boldsymbol{n}_{\dot{\sigma}} = \dot{\boldsymbol{\sigma}}/\mathrm{II}_{\dot{\boldsymbol{\sigma}}}^{1/2}$, of the stress tensor, $\boldsymbol{\sigma}$, can be obtained directly from the experiments. The evolution direction, $\boldsymbol{n}_{\dot{\boldsymbol{e}}_\mathrm{p}} = \dot{\boldsymbol{e}}_{\Delta\mathrm{p}}/\mathrm{II}_{\dot{\boldsymbol{e}}_{\Delta\mathrm{p}}}^{1/2}$, of the plastic strain tensor, $\boldsymbol{e}_{\Delta\mathrm{p}}$, can be obtained by using the identified elastic compliance tensor, i.e.

$$\dot{\boldsymbol{e}}_{\Delta\mathrm{p}} = \dot{\boldsymbol{e}}_{\Delta} - \mathbf{E}^{-1} : \dot{\boldsymbol{\sigma}} \tag{76}$$

When comparing the model prediction with experiments, the direction information in $\dot{\boldsymbol{\sigma}}$ or $\dot{\boldsymbol{e}}_{\Delta\mathrm{p}}$ can be used. But in order to decide the better measure, we have investigated the experimental uncertainty in these directions. Four direction angles, $\alpha_{\dot{\sigma}}, \alpha_{\dot{e}_{\Delta\mathrm{p}}}, \hat{\alpha}_{\dot{\sigma}} = \alpha_{\dot{\sigma}} - \alpha_y$, and $\hat{\alpha}_{\dot{e}_{\Delta\mathrm{p}}} = \alpha_{\dot{e}_{\Delta\mathrm{p}}} - \alpha_y$, are investigated, see Fig. 13.

In order to evaluate the mean value from the experiments, we use experiments that were repeated in the same loading direction for the same predeformation level. The mean angle, $\bar{\alpha}$, and the variation s_α are calculated as

$$\bar{x} = \sum_{i=1}^{N} cos(\alpha_i), \quad \bar{y} = \sum_{i=1}^{N} \sin(\alpha_i) \tag{77}$$

$$\bar{\alpha} = \mathrm{atan2}(\bar{y}, \bar{x}), \quad s_\alpha = 1 - \sqrt{\bar{x}^2 - \bar{y}^2} \tag{78}$$

where atan2 is defined in IEEE (2008). In the study of the experimental uncertainties, we define the yield surface by different von Mises offset strains: 0.01%, 0.05%, 0.1%, 0.2%, and 0.25%. The variations in Table 3 show that the relative stress direction measure, $\hat{\alpha}_{\dot{\sigma}}$, has the lowest variation, and hence will be used in the objective function.

The objective function, $E_\mathrm{y}\left(\underline{\boldsymbol{p}}\right)$, defines the modeling error for the yield points as a function of the material parameters $\underline{\boldsymbol{p}}$, specifically

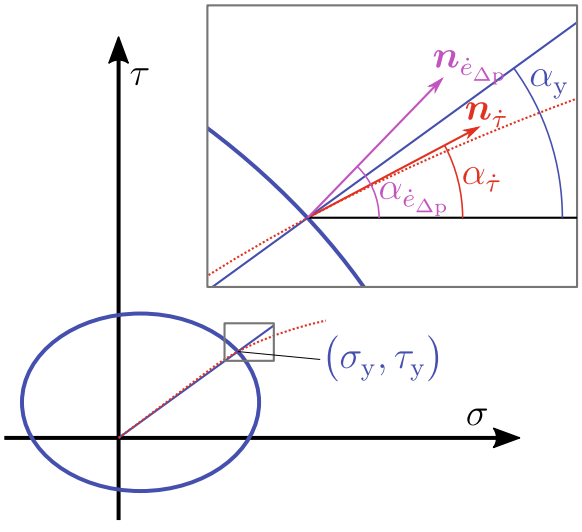

Fig. 13. Directions at yield detection.

Table 3
Experimental variation in directional measures.

Direction measure	$\alpha_{\dot{\sigma}}$	$\alpha_{\dot{e}_{\Delta\mathrm{p}}}$	$\hat{\alpha}_{\dot{\sigma}}$	$\hat{\alpha}_{\dot{e}_{\Delta\mathrm{p}}}$
$s_\alpha \cdot 10^5$	10	16	6	20

$$E_\mathrm{y}\left(\underline{\boldsymbol{p}}\right) = \sum_{\text{all exp points}} \left[\left[\frac{f_{\mathrm{vM}}\left(\boldsymbol{\sigma}_\mathrm{y}^{\mathrm{sim}} - \boldsymbol{\sigma}_\mathrm{y}^{\mathrm{exp}}\right)}{f_{\mathrm{vM}}\left(\boldsymbol{\sigma}_\mathrm{y}^{\mathrm{exp}}\right)} \right]^2 + k_\alpha \left[\hat{\alpha}_{\dot{\sigma}}^{\mathrm{sim}} - \hat{\alpha}_{\dot{\sigma}}^{\mathrm{exp}}\right]^2 \right] \frac{1}{N_{\mathrm{exp}}} \tag{79}$$

where k_α controls the importance of the stress evolution direction. $\bullet^{\mathrm{sim}}$ and $\bullet^{\mathrm{exp}}$ denote the simulated and experimental values respectively. N_{exp} is the number of evaluated experimental yield points. A value of $k_\alpha = 0.3$ was chosen, giving a 5% error for 10° angular error.

Appendix D. Reference model

In this section, we briefly summarize the parts of the reference model that are different in the improved model. The reference model was denoted the Shi model in Meyer (2020) and its complete details are discussed in that work.

The yield function is given as

$$\Phi = \sqrt{\boldsymbol{M}_{\mathrm{red}} : \mathbf{C} : \boldsymbol{M}_{\mathrm{red}}^{\mathrm{t}}} - Y_0 - Y_{\infty,1}\left[1 - \exp\left(\lambda \frac{H_{\mathrm{iso},1}}{Y_{\infty,1}}\right)\right] \tag{80}$$

where the isotropic hardening modulus, $H_{\mathrm{iso},1}$, was introduced. This parameter is equivalent to $Y_{\infty,1}k_{\mathrm{iso},1}$ in the improved model. We show it here as this formulation was used when optimizing the parameters, and a reformulation may affect the optimization results. The main differences between the reference model and the improved model are in the anisotropy tensor, $\mathbf{C}$. The reference model uses $\mathbf{C}$ directly in the yield criterion, while the improved model uses $\mathbf{C}$ to transform the stress tensor and evaluate the von Mises transformed stress. The evolution of $\mathbf{C}$ is similar for both models, except that the reference model also includes the dynamic (self) hardening.

$$\mathbf{C} = \frac{3}{2}\left[[1 - b_\mathrm{L} - b_\mathrm{D}]\mathbf{I}^{\mathrm{dev}} + b_\mathrm{L}\mathbf{C}_\mathrm{L} + b_\mathrm{D}\mathbf{C}_\mathrm{D}\right] \tag{81}$$

$$\dot{\mathbf{C}}_\mathrm{D} = -\dot{\lambda} c_\mathrm{D}\left[\mathbf{N}^{\mathrm{T}} :: \mathbf{C}_\mathrm{D}\right]\mathbf{N}, \tag{82}$$

$$\dot{\mathbf{C}}_\mathrm{L} = -\dot{\lambda} c_\mathrm{L}\left[\mathbf{N}_\perp^{\mathrm{T}} :: \mathbf{C}_\mathrm{L}\right]\mathbf{N}_\perp \tag{83}$$

where $\mathbf{N} = \boldsymbol{N} \otimes \boldsymbol{N}^{\mathrm{t}}$. The initial value of both $\mathbf{C}_\mathrm{D}$ and $\mathbf{C}_\mathrm{L}$ is $\mathbf{I}^{\mathrm{dev}}$. Note that the latent hardening $\mathbf{C}_\mathrm{L}$ in the reference model capture the same phenomena as the cross hardening, $\mathbf{C}_\mathrm{c}$ in the improved model. The parameters associated to the distortional hardening parameters are thus $b_\mathrm{D}, b_\mathrm{L}, c_\mathrm{D}$, and c_L. The elastic law and the kinematic hardening for the reference model are the same as in the improved model.

References

Abel, A., Muir, H., 1972. The Bauschinger effect and discontinuous yielding. Phil. Mag. 26 (2), 489–504.

Advani, S.G., Tucker, C.L., 1987. The use of tensors to describe and predict fiber orientation in short fiber composites. J. Rheol. 31 (8), 751–784.

Advani, S.G., Tucker, C.L., 1990. Closure approximations for three-dimensional structure tensors. J. Rheol. 34 (3), 367–386.

Altan, M.C., Subbiah, S., Güçeri, S.I., Pipes, R.B., 1990. Numerical prediction of three-dimensional fiber orientation in Hele-Shaw flows. Polym. Eng. Sci. 30 (14), 848–859.

Banabic, D., Kuwabara, T., Balan, T., Comsa, D., Julean, D., 2003. Non-quadratic yield criterion for orthotropic sheet metals under plane-stress conditions. Int. J. Mech. Sci. 45 (5), 797–811.

Barlat, F., Aretz, H., Yoon, J., Karabin, M., Brem, J., Dick, R., 2005. Linear transfomation-based anisotropic yield functions. Int. J. Plast 21 (5), 1009–1039.

Barlat, F., Gracio, J.J., Lee, M.-G., Rauch, E.F., Vincze, G., 2011. An alternative to kinematic hardening in classical plasticity. Int. J. Plast 27 (9), 1309–1327.

Barrett, T.J., McCabe, R.J., Brown, D.W., Clausen, B., Vogel, S.C., Knezevic, M., 2020. Predicting deformation behavior of α)uranium during tension, compression, load reversal, rolling, and sheet forming using elasto-plastic, multi-level crystal plasticity coupled with finite elements. J. Mech. Phys. Solids 138, 103924.

Bartels, A., Mosler, J., 2017. On the numerical implementation of thermomechanically coupled distortional hardening. Int. J. Plast 96, 182–209.

Bauschinger, J., 1881. Über die Veränderung der Elasticitätsgrenze und des Elastizitätsmoduls verschiedener Metalle. Der Civilingenieur 27.

Bažant, P., Oh, B.H., 1986. Efficient numerical integration on the surface of a sphere. ZAMM – J. Appl. Math. Mech. 66 (1), 37–49.
Bertram, A., Böhlke, T., 2002. The evolution of the elastic properties of FCC polycrystals due to texture evolution. Mater. Sci. Forum 408–412, 1091–1096.
Böhlke, T., Bertram, A., 2001. The evolution of Hooke's law due to texture development in FCC polycrystals. Int. J. Solids Struct. 38 (52), 9437–9459.
Böhlke, T., Bertram, A., Krempl, E., 2003. Modeling of deformation induced anisotropy in free-end torsion. Int. J. Plast 19 (11), 1867–1884.
Burlet, H., Cailletaud, G., 1986. Numerical techniques for cyclic plasticity at variable temperature. Eng. Comput. 3 (2), 143–153.
Cazacu, O., Chandola, N., Revil-Baudard, B., Frodal, B.H., Børvik, T., Hopperstad, O.S., 2020. Modeling the effect of notch geometry on the deformation of a strongly anisotropic aluminum alloy. European Journal of Mechanics, A/Solids 82 (December 2019), 104004..
Cazacu, O., Rodríguez-Martínez, J.A., 2019. Effects of plastic anisotropy on localization in orthotropic materials: New explicit expressions for the orientation of localization bands in flat specimens subjected to uniaxial tension. J. Mech. Phys. Solids 126, 272–284.
Chaboche, J.L., Van, K.D., Cordier, G., 1979. Modelization of the Strain Memory Effect on the Cyclic Hardening of 316 Stainless Steel. Tech. rep., SMiRT 5, Berlin, Germany..
Dafalias, Y., Rashid, M., 1989. The effect of plastic spin on anisotropic material behavior. Int. J. Plast 5 (3), 227–246.
Dafalias, Y.F., 1983. Corotational rates for kinematic hardening at large plastic deformations. J. Appl. Mech. Trans. ASME 50 (3), 561–565.
Dafalias, Y.F., 1985. The plastic spin. J. Appl. Mech. 52 (4), 865–871.
Dafalias, Y.F., 1993. Planar double-slip micromechanical model for polycrystal plasticity. J. Eng. Mech. 119 (6), 1260–1284.
Dafalias, Y.F., 1998. Plastic spin: necessity or redundancy? Int. J. Plast 14 (9), 909–931.
Dafalias, Y.F., 2001. Orientation distribution function in non-affine rotations. J. Mech. Phys. Solids 49 (11), 2493–2516.
Dafalias, Y.F., Feigenbaum, H.P., 2011. Biaxial ratchetting with novel variations of kinematic hardening. Int. J. Plast 27 (4), 479–491.
Dafalias, Y.F., Schick, D., Tsakmakis, C., 2002. A Simple Model for Describing Yield Surface Evolution During Plastic Flow. Springer, Berlin Heidelberg, Berlin, Heidelberg, pp. 169–201.
Dettmer, W., Reese, S., 2004. On the theoretical and numerical modelling of Armstrong-Frederick kinematic hardening in the finite strain regime. Comput. Methods Appl. Mech. Eng. 193 (1), 87–116.
Dunand, M., Maertens, A.P., Luo, M., Mohr, D., 2012. Experiments and modeling of anisotropic aluminum extrusions under multi-axial loading - Part I: Plasticity. Int. J. Plast 36, 34–49.
Ekh, M., 2001. Thermo-Elastic-Viscoplastic Modeling of IN792. J. Mech. Behav. Mater. 12 (6), 359–388.
Feigenbaum, H.P., Dafalias, Y.F., 2007. Directional distortional hardening in metal plasticity within thermodynamics. Int. J. Solids Struct. 44 (22–23), 7526–7542.
Feigenbaum, H.P., Dafalias, Y.F., 2008. Simple model for directional distortional hardening in metal plasticity within thermodynamics. J. Eng. Mech. 134 (9), 730–738.
Feigenbaum, H.P., Dafalias, Y.F., 2014. Directional distortional hardening at large plastic deformations. Int. J. Solids Struct. 51 (23–24), 3904–3918.
Feigenbaum, H.P., Dugdale, J., Dafalias, Y.F., Kourousis, K.I., Plesek, J., 2012. Multiaxial ratcheting with advanced kinematic and directional distortional hardening rules. Int. J. Solids Struct. 49 (22), 3063–3076.
François, M., 2001. A plasticity model with yield surface distortion for non proportional loading. Int. J. Plast 17 (5), 703–717.
Frederick, C.O., Armstrong, P.J., 2007. A mathematical representation of the multiaxial Bauschinger effect. Mater. High Temp. 24 (1), 1–26.
Ghosh, G., 2015. A first-principles study of cementite (Fe3C) and its alloyed counterparts: Elastic constants, elastic anisotropies, and isotropic elastic moduli. AIP Adv. 5, (8) 087102.
Harrysson, M., Ristinmaa, M., 2008. Two different approaches to model evolving directional properties at finite deformations. Acta Mech. 199 (1–4), 97–116.
Hasegawa, T., Yakou, T., Kocks, U.F., 1986. Forward and reverse rearrangements of dislocations in tangled walls. Mater. Sci. Eng. 81, 189–199.
Hill, R., 1948. A theory of the yielding and plastic flow of anisotropic metals. Proc. R. Soc. A 193 (1033), 281–297.
Holmedal, B., 2019. Bauschinger effect modelled by yield surface distortions. Int. J. Plast 123, 86–100.
IEEE 1003.1-2008, 2008. Standard for Information Technology- Portable Operating System Interface (POSIX)..
Ishikawa, H., Sasaki, K., 1988. Yield Surfaces of SUS304 Under Cyclic Loading. J. Eng. Mater. Technol. 110 (4), 364–371.
ISO 10113:2020, 2020. Metallic materials – Sheet and strip – Determination of plastic strain ratio..
Jack, D.A., Smith, D.E., 2006. Sixth-order fitted closures for short-fiber reinforced polymer composites. J. Thermoplast. Compos. Mater. 19 (2), 217–246.
Jeong, Y., Barlat, F., Tomé, C.N., Wen, W., 2017. A comparative study between micro- and macro-mechanical constitutive models developed for complex loading scenarios. Int. J. Plast 93, 212–228.
Johansson, G., Ekh, M., 2006. On the modeling of evolving anisotropy and large strains in pearlitic steel. Eur. J. Mech. A Solids 25 (6), 1041–1060.
Johansson, G., Menzel, A., Runesson, K., 2005. Modeling of anisotropic inelasticity in pearlitic steel at large strains due to deformation induced substructure evolution. Eur. J. Mech. A Solids 24 (6), 899–918.
Kaiser, T., Lu, J., Menzel, A., Papadopoulos, P., 2020. A covariant formulation of finite plasticity with plasticity-induced evolution of anisotropy: modeling, algorithmics, simulation, and comparison to experiments. Int. J. Solids Struct. 185–186, 116–142.
Kocks, U.F., Mecking, H., 2003. Physics and phenomenology of strain hardening: The FCC case. Prog. Mater Sci. 48 (3), 171–273.
Korelc, J., 2002. Multi-language and Multi-environment Generation of Nonlinear Finite Element Codes. Eng. Comput. 18 (4), 312–327.
Kratochvil, J., 1971. Finite-Strain Theory of Crystalline Elastic-Inelastic Materials. J. Appl. Phys. 42 (3), 1104–1108.
Kurtyka, T., Zyczkowski, M., 1996. Evolution equations for distortional plastic hardening. Int. J. Plast 12 (2), 191–213.
Kweon, S., 2013. Investigation of shear damage considering the evolution of anisotropy. J. Mech. Phys. Solids 61 (12), 2605–2624.
Larijani, N., Johansson, G., Ekh, M., 2013. Hybrid micro-macromechanical modeling of anisotropy evolution in pearlitic steel. Eur. J. Mech. A Solids 38, 38–47.
Lu, J., Papadopoulos, P., 2004. A covariant formulation of anisotropic finite plasticity: Theoretical developments. Comput. Methods Appl. Mech. Eng. 193 (48–51), 5339–5358.
Man, C.S., 1995. On the correlation of elastic and plastic anisotropy in sheet metals. J. Elast. 39 (2), 165–173.
Mandel, J., 1971. Plasticite Classique et Viscoplasticite (Tech. rep.). International Center for Mechanical Sciences, Springer, New York.
Mandel, J., 1973. Equations constitutives et directeurs dans les milieux plastiques et viscoplastiques. Int. J. Solids Struct. 9 (6), 725–740.
Masing, G., 1926. Eigenspannungen und Verfestigung beim Messing. In: 2nd International Congress of Applied Mechanics, pp. 332–335.
Menzel, A., Ekh, M., Runesson, K., Steinmann, P., 2005. A framework for multiplicative elastoplasticity with kinematic hardening coupled to anisotropic damage. Int. J. Plast 21 (3), 397–434.
Menzel, A., Harrysson, M., Ristinmaa, M., 2008. Towards an orientation-distribution-based multi-scale approach for remodelling biological tissues. Comput. Methods Biomech. Biomed. Eng. 11 (5), 505–524.
Menzel, A., Steinmann, P., 2003. On the spatial formulation of anisotropic multiplicative elasto-plasticity. Comput. Methods Appl. Mech. Eng. 192 (31–32), 3431–3470.
Menzel, A., Waffenschmidt, T., 2009. A microsphere-based remodelling formulation for anisotropic biological tissues. Philos. Trans. R. Soc. A 367 (1902), 3499–3523.
Méric, L., Poubanne, P., Cailletaud, G., 1991. Single crystal modeling for structural calculations: Part 1 – model presentation. J. Eng. Mater. Technol. 113 (1), 162–170.
Meyer, K.A., 2019. matmodfit.https://github.com/KnutAM/matmodfit. .
Meyer, K.A., 2020. Evaluation of material models describing the evolution of plastic anisotropy in pearlitic steel. Int. J. Solids Struct. 200–201, 266–285.
Meyer, K.A., Ekh, M., 2017. A comparison of two frameworks for kinematic hardening in hyperelasto-plasticity. In: O nnate, E., Owen, D., Peric, D., Chiumenti, M. (Eds.), XIV International Conference on Computational Plasticity. Fundamentals and Applications. COMPLAS XIV, Barcelona, pp. 342–350..
Meyer, K.A., Ekh, M., Ahlström, J., 2018a. Modeling of kinematic hardening at large biaxial deformations in pearlitic rail steel. Int. J. Solids Struct. 130–131, 122–132.
Meyer, K.A., Ekh, M., Ahlström, J., 2019. Material model calibration against axial-torsion-pressure experiments accounting for the non-uniform stress distribution. Finite Elem. Anal. Des. 163, 1–13.
Meyer, K.A., Ekh, M., Ahlström, J., 2020. Anisotropic yield surfaces after large shear deformations in pearlitic steel. Eur. J. Mech. A. Solids 82, 103977.
Meyer, K.A., Ekh, M., Brouzoulis, J., Ahlström, J., 2015. Modeling of Anisotropy Evolution in Pearlitic Steel. In: Berezovski, A., Tamm, K., Peets, T. (Eds.), 28th Nordic Seminar on Computational Mechanics. Tallinn, pp. 111–114. .
Meyer, K.A., Nikas, D., Ahlström, J., 2018b. Microstructure and mechanical properties of the running band in a pearlitic rail steel: Comparison between biaxially deformed steel and field samples. Wear 396–397, 12–21.
Naghdi, P.M., Essenburg, F., Koff, W., 1958. An experimental study of initial and subsequent yield surfaces in plasticity. J. Appl. Mech. 25 (2), 201–209.
Nelder, J.A., Mead, R., 1965. A simplex method for function minimization. Comput. J. 7 (4), 308–313.
Noman, M., Clausmeyer, T., Barthel, C., Svendsen, B., Huétink, J., van Riel, M., 2010. Experimental characterization and modeling of the hardening behavior of the sheet steel LH800. Mater. Sci. Eng. A 527 (10–11), 2515–2526.
Ortiz, M., Popov, E.P., 1983. Distortional hardening rules for metal plasticity. J. Eng. Mech. 109 (4), 1042–1057.
Papadopoulos, P., Lu, J., 2001. On the formulation and numerical solution of problems in anisotropic finite plasticity. Comput. Methods Appl. Mech. Eng. 190 (37–38), 4889–4910.
Pham, M.S., Creuziger, A., Iadicola, M., Rollett, A.D., 2017. Roles of texture and latent hardening on plastic anisotropy of face-centered-cubic materials during multi-axial loading. J. Mech. Phys. Solids 99, 50–69.
Phillips, A., Juh-Ling, T., 1972. The effect of loading path on the yield surface at elevated temperatures. Int. J. Solids Struct. 8 (4), 463–474.
Pietryga, M.P., Vladimirov, I.N., Reese, S., 2012. A finite deformation model for evolving flow anisotropy with distortional hardening including experimental validation. Mech. Mater. 44, 163–173.
Plesek, J., Feigenbaum, H.P., Dafalias, Y.F., 2010. Convexity of yield surface with directional distortional hardening rules. J. Eng. Mech. 136 (4), 477–484.

Qin, J., Holmedal, B., Hopperstad, O.S., 2018. A combined isotropic, kinematic and distortional hardening model for aluminum and steels under complex strain-path changes. Int. J. Plast 101, 156–169.
Qin, J., Holmedal, B., Hopperstad, O.S., 2019. Experimental characterization and modeling of aluminum alloy AA3103 for complex single and double strain-path changes. Int. J. Plast 112, 158–171.
Qin, J., Holmedal, B., Zhang, K., Hopperstad, O.S., 2017. Modeling strain-path changes in aluminum and steel. Int. J. Solids Struct. 117, 123–136.
Quey, R., Villani, A., Maurice, C., 2018. Nearly uniform sampling of crystal orientations. J. Appl. Crystallogr. 51, 1162–1173.
Shi, B., Bartels, A., Mosler, J., 2014. On the thermodynamically consistent modeling of distortional hardening: A novel generalized framework. Int. J. Plast 63, 170–182.
Skelton, R., Maier, H., Christ, H.-J., 1997. The Bauschinger effect, Masing model and the Ramberg-Osgood relation for cyclic deformation in metals. Mater. Sci. Eng.: A 238 (2), 377–390.
Sung, S.-J., Liu, L.-W., Hong, H.-K., Wu, H.-C., 2011. Evolution of yield surface in the 2D and 3D stress spaces. Int. J. Solids Struct. 48 (6), 1054–1069.
Sweeney, C., Vorster, W., Leen, S., Sakurada, E., McHugh, P., Dunne, F., 2013. The role of elastic anisotropy, length scale and crystallographic slip in fatigue crack nucleation. J. Mech. Phys. Solids 61 (5), 1224–1240.
Swift, H.W., 1947. Length changes in metals under torsional overstrain. Engineering 163, 253–257.
Teodosiu, C., Hu, Z., 1995. Evolution of the intragranular microstructure at moderate and large strains: Modelling and computational significance. In: Shen, S., Dawson, P. (Eds.), Proceedings of Numiform'95 on Simulation of Materials Processing: Theory, Methods and Applications. Rotterdam, pp. 173–182..
Voyiadjis, G.Z., Foroozesh, M., 1990. Anisotropic distortional yield model. J. Appl. Mech. Trans. ASME 57 (3), 537–547.
Wallin, M., Ristinmaa, M., 2005. Deformation gradient based kinematic hardening model. Int. J. Plast 21 (10), 2025–2050.
Wallin, M., Ristinmaa, M., Ottosen, N.S., 2003. Kinematic hardening in large strain plasticity. Eur. J. Mech. A. Solids 22 (3), 341–356.
Wang, J., Levkovitch, V., Reusch, F., Svendsen, B., Huétink, J., van Riel, M., 2008. On the modeling of hardening in metals during non-proportional loading. Int. J. Plast 24 (6), 1039–1070.
Wicht, D., Schneider, M., Böhlke, T., 2020. On Quasi-Newton methods in fast Fourier transform-based micromechanics. Int. J. Numer. Meth. Eng. 121 (8), 1665–1694.
Wu, H.-C., Hong, H.-K., Lu, J.-K., 1995. An endochronic theory accounted for deformation induced anisotropy. Int. J. Plast 11 (2), 145–162.
Yang, C., Shi, B., Peng, Y., Pan, F., 2018. Transition from convex to concave of equal plastic work contours for wrought magnesium alloy under multi-axial loading. Int. J. Solids Struct. 150, 117–124.
Zhang, H., Diehl, M., Roters, F., Raabe, D., 2016. A virtual laboratory using high resolution crystal plasticity simulations to determine the initial yield surface for sheet metal forming operations. Int. J. Plast 80, 111–138.